Fabrication and Characterization of Novel Flow Battery Electrodes using Electrospinning

by

Shashi Yadav

A thesis

presented to the University of Waterloo

in fulfilment of the

thesis requirement for the degree of

Master of Applied Science

in

Chemical Engineering

Waterloo, Ontario, Canada, 2018

Author’s Declaration

I hereby declare that I am the sole author of this thesis. This is a true copy of the thesis, including any required final revisions, as accepted by my supervisor and examiners.

I understand that my thesis may be made electronically available to the public.

Statement of Contributions

The electrospinning set-up used in this study was designed by Matt Kok. Permeability and electrical conductivity measurement devices were designed by other members of the PMEAL team. The flow battery test was conducted by Brushett Research Group members Antoni Forner Cuenca and Kevin Michael Tenny at MIT.

Abstract

The increase in energy demand, depletion of fossil fuel reserves and climate change has shifted our focus to using renewable energy resources. Alternative energy sources, though environmentally friendly, are intermittent and thus require large-scale energy storage to buffer the temporal mismatch between power generation and power consumption. Flow batteries are a leading candidate for this role due to their decoupled energy and power capacity. The energy and power density of flow batteries are generally lower than that of lead-acid, lithium-ion and nickel metal hydride batteries. Improving electrode properties and structure can lead to increased power density of flow batteries. Instead of modifying the commercially available carbon paper, this study focused on fabricating electrodes using electrospinning. A novel technique was developed to make electrodes composed of flat fibres relative to commonly used cylindrical fibre electrodes. The electrodes were then characterized for various properties such as fibre size, porosity, surface area, permeability and electrical conductivity. The change in fibre morphology led to an increase in reactive surface area and permeability of the electrode. This can help to improve reaction kinetics and mass transport in electrodes and thereby the power density and performance of flow batteries.

Acknowledgements

I would like to sincerely thank my supervisor, Professor Jeff Gostick for giving me an opportunity to work under his supervision. He has been extremely patient and motivating when things weren't going right. I would like to thank him for calming me down when I damaged the tube furnace and telling me that it was okay. A big thanks to Matt for guiding me and explaining all about electrospinning. Thank you for helping me reassemble the electrospinning equipment and for troubleshooting problems. He never forgot to ask me how things were going and for telling me to be patient when nothing seemed to work. I would like to thank all my teammates: Yong for getting me started in the lab when I joined PMEAL, Tom for helping me understand electrical conductivity experiment and Awais for investing so much of his time and effort in fixing the furnace that I broke and for training me on using DVS instrument.

Thanks to Bert for taking out the time to make the box for electrospinning, Lei for helping me numerous times with SEM and the entire administrative staff for answering my questions.

I would like to acknowledge Sunny's support at every step of my research and his words of encouragement to lift me up when I felt low. He has always been a constant source of support. I would like to thank my friend Aishwarya who knew how to get me on track and for taking out the time when I needed her and Arshdeep for always cheering me up and helping me whenever possible. My sincere thanks to Muneedra and Kiana for helping me along the way.

I would also like to thank my family for their support, especially my loving parents who made countless sacrifices to help me achieve my dreams and for being my motivation. Last but not the least, to Almighty for his grace as none of this would have been possible without him.

Table of Contents

List of Figures

List of Tables

List of Abbreviations

CAES	Compressed Air Energy Storage
CS	Core Solution
DCM	Dichloromethane
DMF	N,N-Dimethylformamide
ES	Electrospinning
RFB	Redox Flow Battery
FFs	Flat Fibres
ICR	Iron Chromium Redox
IEA	International Energy Agency
MWCNTs	Multi Wall Carbon Nanotubes
NFs	Nanofibres
PAN	Polyacrylonitrile
PDT	Poly(dodecylthiophene)
PEMFCs	Proton Exchange Membrane Fuel Cells
PEO	Poly(ethylene oxide)
PHES	Pumped Hydro Energy Storage
PS	Polystyrene
PSB	Polysulfide Bromide
RFB	Redox Flow Battery
SA	Surface Area
SS	Shell Solution
VRFB	Vanadium Redox Flow Battery

1 Introduction

1.1 Motivation

Relentless growth in energy demand has been observed over the past two decades, mainly because of the rising population and economic growth, especially in emerging market economies such as China and India. According to the International Energy Agency, global energy demand increased by 2.1% in 2017 in comparison to a 0.9% increase in 2016 and 0.9% average annual increase over the past 5 years [1]. The importance of electricity in energy use across the globe is also rising. The amount of electricity generated reached an all-time high of 25570 TWh in 2017. The graph below shows the significant increase in global electricity production from 2000-2017.

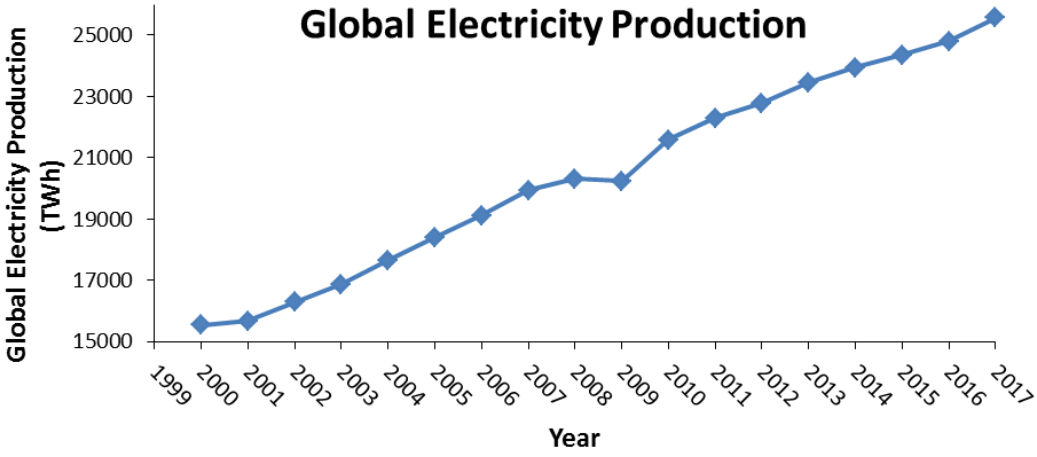

Figure 1: Global Electricity Production from 2000-2017 [1], [2].

To date, fossil fuels continue to play a major role in electricity generation. In 2017, 65% of the world electricity was produced by coal, oil and natural gas combined. The pie-chart in Figure 2 shows the contribution of the various sources for electricity generation in 2017, of which renewables make up only 25%.

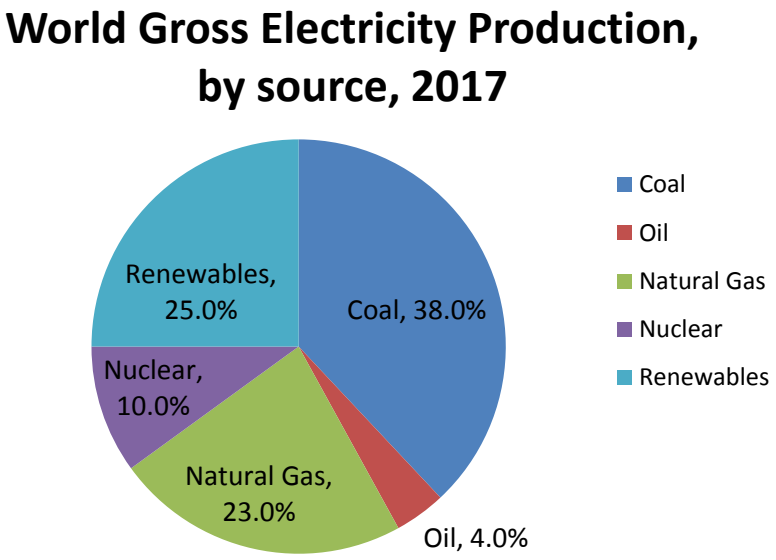

Figure 2: Global Electricity Production by Source in 2017 [1].

The increased use of fossil fuels has led to air pollution and CO_2 emissions. In order to mitigate pollution and climate change, research and development is underway to develop efficient technologies to generate electricity from renewable energy sources such as hydro, solar power, wind power, tidal power, etc. Currently, hydropower is the largest renewable source for electricity generation, amounting to a share of 65% in 2017 [1]. However, hydro-power is strongly constrained by geography. Thus, the solution to decrease fossil fuel use and CO_2 emissions lies in the expanded installation of solar and wind power technologies and their integration into the current grid system. The problem with these technologies is that the wind does not always blow and the sun does not always shine so power generation does not always match power demand. Moreover, the mismatch between power generation and power demand can cause frequency deviations during electric power generation. This variation in frequency can damage power plant auxiliaries such as turbines, generators and transformers and therefore adversely affect the stability of transmission systems. According to Weber *et al*, if non-dispatchable renewable energy exceeds 20% of the grid generation capacity without energy storage, then it can destabilize the grid [3].

Thus, large scale energy storage devices are required to store excess energy obtained from renewables. Background of various large scale energy storage devices along with their advantages and limitations is provided in Chapter 2. This thesis focuses on use of flow battery as a large scale energy storage device because of its unique ability to decouple power and energy components and geographical flexibility [4]–[7].

1.2 Flow Batteries

Redox flow batteries are a promising option due to their decoupled energy and power capacity, geographic and chemical flexibility and ease of scale-up [3], [8]. A typical flow battery configuration is shown in Figure 3.

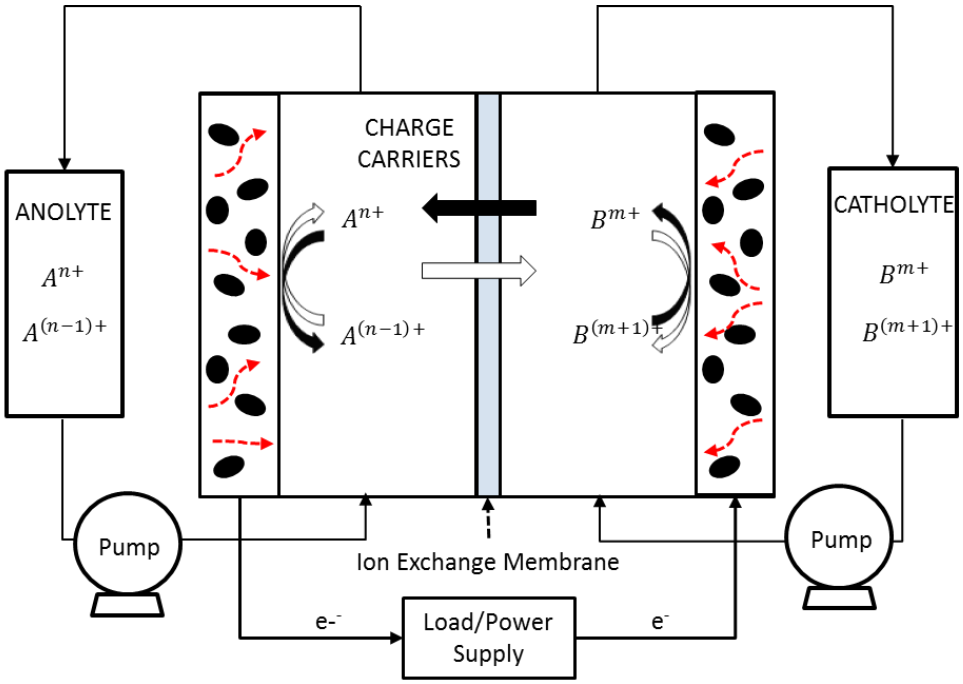

Figure 3: Flow Battery Setup.

A flow battery cell consists of two electrodes in contact with electrolytes with different composition that are separated by an ion exchange membrane. Electro-active material is dissolved in each electrolyte and stored in external storage tanks, unlike conventional batteries that store electro-active material in electrodes. During charge/discharge, electrolyte is pumped into each cell compartment and reduction/oxidation

reactions occur at the cathode and anode surface. The electrons flow through the external circuit and ions across the membrane. The following hypothetical reactions occur in a generic flow battery [9]:

$$A^{n+} + xe^- \xrightarrow{charge} A^{(n-x)+} \; ; \; A^{(n-x)+} \xrightarrow{discharge} A^{n+} + xe^-$$

$$B^{m+} \xrightarrow{charge} B^{(m+y)+} + ye^- \; ; B^{(m+y)+} + ye^- \xrightarrow{discharge} B^{m+}$$

Energy and power density are two important performance factors of flow batteries. The energy density [J/m^3] or capacity depends on electrolyte concentration, whereas the power density [W/m^3] depends on the stack size. This decoupled nature of energy and power enables these two properties to be independent of each other. For instance, an increase in the concentration of electro-active material in the electrolyte can enhance energy density. A high concentration of redox compounds enables more electrons to be exchanged for a given volume of electrolyte, leading to higher capacity and energy density [10]. The total power output, on the other hand, is proportional to the number of cells in the stack [10]. However, an increase in the number of cells also increases the cost. A study conducted by Zhang and co-workers showed that the stack is one of the major cost components, accounting for 31% of the capital cost of a base case vanadium redox flow battery [11]. Minimization of the installed cost of RFBs is imperative to accelerate their commercialization for energy storage. Increasing power density by optimizing electrode configuration or by decreasing the cell size for a given power output are effective ways of decreasing cost [11]. A third approach to this problem is to more efficiently operate cells at a higher power density so that more energy can be stored and extracted from the electrolyte and the energy density of the system can be increased. Efforts to improve the performance of RFBs have largely been focused on increasing RFB energy density [10], with less attention on enhancing their power density.

1.3 Objectives

The commercially used electrodes (SGL25AA) in flow batteries have high permeability but low surface area (m^2/m^3) because of their large fibre size. Thus, these off-the shelf materials have good mass transfer properties but poor kinetic performance which adversely affects the power density of flow batteries. This thesis focuses on enhancing the power density of flow batteries by improving electrode kinetics and minimizing mass transfer losses at electrodes. Kinetics can be improved by increasing the surface area of electrodes or by enhancing electrode activity. Mass transfer losses can be decreased by increasing the porosity and permeability of electrodes.

Attempts made by researchers to enhance reaction kinetics by increasing electrode activity focus on the catalyst at the electrode surface [12]. Thermal or chemical treatment is another technique that increases electrode surface activity [13] by increasing the number of functional groups on the electrode surface [12].

Some of the methods that have been investigated to enhance kinetics by increasing electrode surface area are to stack together multiple layers of carbon paper electrodes [13]. This will increase the overall thickness of the cathode/anode. Increase in thickness of electrode is less than ideal since this will increase the distance that needs to be travelled by ionic species to reach reactive sites thus increasing ohmic losses in the cell. Zhou *et al* tried to increase the surface area of a carbon paper electrode by treating it with KOH to roughen the surfaces. The treatment increased the surface area of carbon paper from 2.39 m^2/g to 15.4 m^2/g by creating nano-pores on the surface of carbon fibre [12]. Although the formation of nano-pores increases the surface area, it is likely that some of the extra surface area provided by nano-pores is not utilized by the electrode reaction because electrolyte cannot flow into such tiny pores. The additional SA associated with the nano-pores can only be reached by relatively slow diffusion processes, making their access mass transfer limited. Various other

attempts that have been made include coating high SA materials such as carbon nano-tubes (CNTs), graphenes, carbon blacks, etc onto the surface of carbon fibres using dip coating or chemical vapour deposition (CVD) techniques. The principal disadvantage of dip coating is that high SA material and carbon fibre are held together by weak van der Waal forces. Electrolyte flowing through the electrode can easily detach them and cause serious durability problems. CVD, on the other hand, attaches high SA material to CNFs with covalent bonds but is costly, complex, tedious and time consuming. This can also decrease electrode permeability which will result in concentration loss and poor cell performance [14]. If permeability decreases, then electrolyte transport will not be good and some of the added surface area might actually remain unused. The low specific surface area of electrodes is thus a major issue for developing high-power RFBs and is yet to be fully resolved due to its competition with the transport properties of the electrode [14].

It is important to note that in all the techniques mentioned above, researchers tried to increase the SA of commercially available carbon paper. Kok *et al* utilized multi-physics modelling to determine the optimum physical properties of fibrous electrodes that are required to improve performance of flow batteries. Their results suggested that a fibre diameter of around 1 to 2 μm coupled with a high porosity of above 80% can help in achieving high power density [15]. These optimal properties reported were very different from those of commercially available carbon paper which have a fibre diameter of around 10 μm and porosity below 75% [16].

To test whether the model predictions were correct or not, Liu *et al* determined the electrospinning conditions at which the resulting fibrous mat has a porosity of ~ 90% and fibres have size 1-2μm [17]. They electrospun fibres possessing these properties and then compared their effectiveness in an all-vanadium RFB to that of commercial carbon paper (SGL25AA). Comparison of the performance curves of both electrodes showed that the

electrospun electrodes prepared with the optimum conditions exhibited better kinetics and higher power density [17]. Thus, electrospinning fibres smaller in size than that of off-the-shelf material can increase the SA and improve kinetics while at the same time maintaining high porosity and reasonable permeability for good mass transport.

This thesis focuses on improving kinetics even further by increasing surface area per unit volume of the electrode (m^2/m^3) while still maintaining considerable porosity and therefore permeability values suitable for good transport of electrolyte. Two parallel approaches are considered. In the first part, various techniques are investigated to make flat fibres. This is done to develop a proof-of-concept material to demonstrate that the change from cylindrical to flat morphology can significantly increase the surface area-to-volume ratio. The second part examines whether an electrode made of highly aligned cylindrical fibres can significantly increase permeability.

1.4 Outline of Thesis

This thesis focuses on improving power density of flow batteries by improving the porous structure of electrodes to have higher surface area without decreasing permeability. Two separate studies are conducted in this regard. One study focuses on enhancing kinetics by increasing surface area per unit volume of the electrode. The other study aims to improve mass transfer in electrodes by increasing their permeability.

Chapter 2 gives background information on the various large scale energy storage technologies and explains why flow batteries are a promising option for use at grid scale. This section is followed by a detailed literature review on flow batteries that provides information about its development phase and the advancements made in investigating new electro-active species and electrolytes to improve RFB performance. The common losses that occur in batteries are also briefly explained. The next section explains the important transport properties of a flow battery electrode and their effect on mass transport and other

performance factors. Since this project focuses on the electrospinning technique to make electrodes, background of this technology is provided in section 2.4 along with information on the various fibrous morphologies that can be fabricated using this method, with a focus on flat fibre morphology and aligned fibres. The non-conductive electrospun fibrous mats are carbonized in a furnace to make them conductive. The important steps and reactions involved in carbonization are covered in section 2.5.

Chapter 3 provides details about the materials used, experimental setup, electrospinning conditions used in each method and characterization techniques used. Chapter 4 and 5 provide information about the development and analysis of the properties of flat fibres electrode and aligned fibres electrode, respectively.

Finally, Chapter 6 summarizes the results of this thesis and provides direction for future work.

2 Background

2.1 Overview of Large Scale Energy Storage Technologies

The increasing penetration of intermittent renewable energy sources into the current grid system gives rise to the problem of imbalance between power supply and power demand. Thus, large scale energy storage devices are needed to ensure a continuous electricity supply by storing energy when available and delivering it when required.

The only known technology able to store electricity directly is capacitors, which have very low energy density. It is thus converted into some other form of energy and then stored. Based on the form in which electricity is stored, energy storage devices can be divided into different categories as shown in Figure 4:

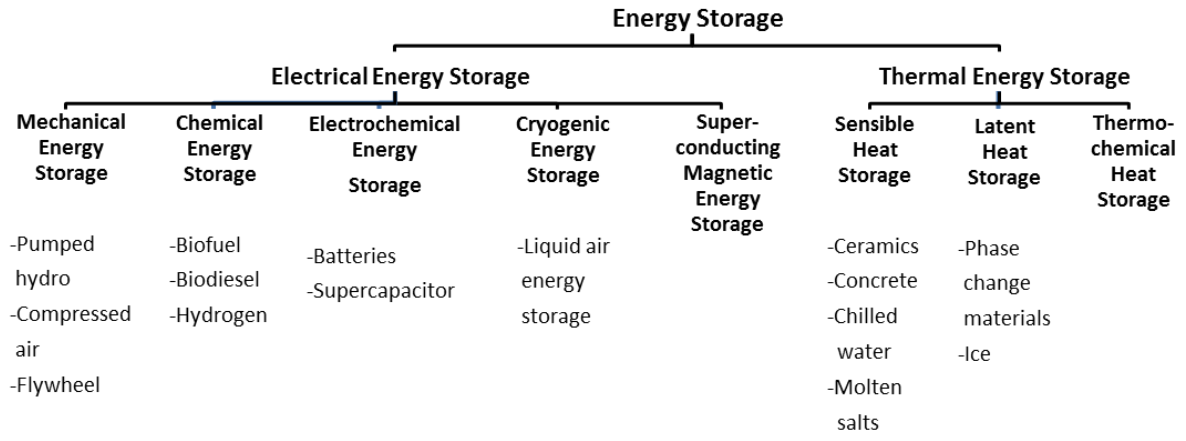

Figure 4: Classification of Energy Storage Technologies [18].

Among the various energy storage devices, pumped hydro energy storage (PHES) is by far the most developed and widely used large scale energy storage technology [8], [18], [19]. According to a survey conducted by the Electric Power Research Institute (EPRI) in 2010, PHES makes up more than 99% of the global large scale energy storage installation. This technology uses off-peak electricity to pump water uphill and store it in reservoirs. The potential energy of water is converted to electrical energy by releasing water downhill to drive turbines, when electricity is needed [20], [21]. It is capable of providing reliable power

[18], but cannot respond to fast power demand [8]. Furthermore, it has special geographical requirements that cannot be met everywhere [8], [18], [22].

Compressed air energy storage is another technology that is commercially used for bulk energy storage. It utilizes off-peak electricity to compress air and store it in a reservoir (eg., underground hard rock cavern, salt cavern or depleted gas field). During peak hours, the gas stored is heated and expanded through a high pressure turbine to generate electricity [23]. CAES has an estimated efficiency of 70% with an expected lifetime of about 40 years [18]. However, as with PHES, CAES also has special geographical requirements that tend to limit its use [8].

Hydrogen electrolysis is another large scale energy storage technology that is gaining increased attention. During periods of low demand, the excess electricity generated by renewables is utilized to produce hydrogen by electrolysis of water. The hydrogen produced from renewables is referred to as "green hydrogen" as the only by-product of this method is water [24], [25]. The gas produced can be stored in a gaseous as well as liquid phase or it can be converted into solid hydride complexes. During peak hours, hydrogen can be used to generate electricity by various methods such as turbines (thermal conversion units) or in fuel cells to make electricity directly and thus help stabilize grids [25], [26]. The National Wind Technology Center near Boulder, Colorado uses electricity generated by wind power and photovoltaic arrays to produce hydrogen gas [27]. This technology is easy to scale and can store large amounts of energy for long periods. Its limitations include the high capital cost of electrolysers and low round trip efficiency, especially using the thermal route [28]**.**

All the above mentioned storage technologies have particular advantages and disadvantages. PHES and CAES are able to store energy at the grid level for long durations but their special site requirements are a hindrance. Hydrogen electrolysis requires more research and development. In this context, electrochemical energy storage devices that are

capable of storing energy over short to long-time scales seem to be the most viable storage technology form at the grid level. What makes them even more attractive is their site versatility, ease of operation and modularity that allows wide scalability [8]. Some examples of electrochemical devices are lead-acid batteries, lithium-ion batteries and redox flow batteries.

The traditional lead-acid batteries appear to be a viable option for use at grid scale because of their low cost, but their self-discharge problem and poor cycle life are a concern [29], [30]. Although lithium-ion batteries have high power density, overheating is a serious safety concern [31] that can result in a decrease in their performance in terms of capacity loss, undesirable side reactions and failure [29], [32]. In the above mentioned conventional batteries, the electro-active material is stored in electrodes. To increase the energy capacity of these batteries, thicker or generally larger electrodes are required. But increasing thickness also increases resistance to electron and mass transport and consequently increases the voltage drop and power loss [33], [34]. Thus, in a conventional battery, a trade-off has to be made between high power (which requires thin electrode) and high energy (which requires thicker electrode) [35], [36].

This problem is resolved in flow batteries because of their decoupled energy and power capacity feature. The amount of energy stored can be raised by increasing the concentration of reactants or the volume of electrolyte stored [35]. Electrode thickness does not have to be varied to enhance energy capacity as in conventional batteries. The power density can be raised by increasing the stack size or by improving its design [35]. In other words, a flow battery can theoretically offer both high power density and large energy capacity in a single device [36]. Also, flow battery electrodes do not participate in reactions as is the case in conventional batteries and simply serve as a substrate for the redox reactions to take place. Thus, they do not expand and contract during repeated charge/discharge cycles

and thus have longer cycle lives [36]. Lead-acid and lithium-ion batteries have cycle lives ranging from 200-2000 cycles and 500-2000 cycles respectively, whereas vanadium redox flow battery is known to have cycle life greater than or equal to 16000 cycles [29], [37]. Also, storing electrolytes separately in external tanks and flowing them through the cell when required eliminates self-discharge issues [35], facilitates thermal management and improves battery safety which is especially important for large-scale electrical energy storage applications [36].

Among the currently available large scale energy storage technologies, redox flow battery appears to be the most promising candidate because of its unlimited capacity, design flexibility and scalability, long lifetime, safety and geographical flexibility [38], [39].

2.2 Flow Batteries History, Classification and Chemistries

In 1949, Kangro patented a battery type similar to the current flow batteries [40]. He used $Cr_2(SO_4)_3$ as the cathode and anode active material and 2M sulphuric acid as the supporting electrolyte. The next big step towards developing flow batteries was taken by the US National Aeronautics and Space Administration (NASA) in the 1970's. The system employed iron-chromium redox couples supported by an acidic electrolyte. However, the cross-over of redox-active species across the membrane prevented further progress in this field. This state of affairs remained unchanged until Skyllas-Kazacos *et al*. built a prototype of a vanadium redox flow battery in the 1980s that utilized VO_2^{+}/VO^{2+} // V^{3+}/V^{2+} as the redox couples. This resolved the problem of species cross-over and capacity decay since similar electrolytes were used in both half-cells [41].

Flow batteries can be classified in two categories: true and hybrid types. In a true flow battery, all the active redox species are stored in electrolytes external to the power conversion device instead of being stored as solid electrodes. Some examples of true flow batteries are the all-vanadium, polysulfide bromide and iron-chromium systems. Hybrid flow batteries on

the other hand store at least one of its electro-active species internally in a solid form. Examples include zinc-bromine and zinc-chlorine batteries [41], [42].

Extensive work has been done to explore the possibility of using a variety of electro-active materials in RFBs to enhance their energy density and improve cell performance. It includes using inorganic redox species [43], which are far more established today, as well as organic components [44], [45] which are relatively new. Non-aqueous electrolytes have also been investigated along with aqueous electrolytes.

The vast majority of flow batteries use inorganic species and aqueous electrolytes. Aqueous electrolytes are not flammable and therefore ensure safe battery operation [41]. Some examples include the iron-chromium (ICR), polysulfide-bromide (PSB) and all-vanadium systems. The PSB system offers several advantages such as low cost, easily available reactants and high solubility of both polysulfides and bromine polysulfides in aqueous electrolytes. An electrical storage facility based on PSB battery was constructed by Regenesys Technologies at Little Barford site in UK in 2002 [46]. Flow batteries employing this chemistry face the problem of species crossover that decreases the capacity and efficiency of the cell. This problem is resolved in all vanadium RFBs which are undoubtedly the most well-known system [47]. The electrochemical reactions involved are [46]:

Positive Electrode:	$VO_2^+ + 2H^+ + e^- \Leftrightarrow VO^{2+} + H_2O$	E^o = +1.00V
Negative Electrode:	$V^{3+} + e^- \Leftrightarrow V^{2+}$	E^o = -0.26V
Overall Reaction:	$VO_2^+ + V^{2+} + 2H^+ \Leftrightarrow VO^{2+} + V^{3+} + H_2O$	E_{cell} = 1.26V

However, the high cost and the low energy density (< 25 Wh/L) because of the low solubility of $VOSO_4$ (< 1.7 M) are the main drawbacks of this system. Also, vanadium is relatively toxic. Nonetheless, several VRFB plants have been installed [47], including the 200 kW/800 kWh system installed in 1996 by Mitsubishi Chemicals at Kashima-Kita Electric Power,

Japan, for load-leveling, a 250 kW/500 kWh battery installed in 2001 by VRB Power at Stellenbosch University, South Africa and a 250 kW/1 MWh system installed in 2003 by Pinnacle VRB for Hydro Tasmania at Huxley Hill Wind Farm on King Island for wind energy storage and diesel fuel replacement. The 4 MW/6 MWh VRFB plant installed by Sumitomo Electric Industries (SEI) for J-Power in 2005 completed more than 270,000 cycles over a period of 3 years, exhibiting excellent performance in smoothing the power output fluctuations at the Subaru Wind Villa Power Plant [8].

More recently, organic electro-active materials have started gaining attention as they offer several advantages over inorganic redox species. Organic compounds are readily available compared to inorganic elements such as vanadium and are relatively inexpensive since they are made of earth abundant elements (carbon, hydrogen, oxygen, nitrogen, sulfur, etc.). In addition, their molecular structure can be altered to achieve desired electrochemical and physical properties (e.g., redox potential, solubility). Moreover, a number of organics are known to exchange two electrons (e.g., quinones), which leads to higher intrinsic capacities and potentially higher cell energy densities [47]. However, the stability of organic species in acidic environment requires further research.

A promising alternative was proposed by Chiang and co-workers by introducing the concept of slurry electrolytes. These batteries offer the high energy density features of lithium-ion batteries in combination with the scalability and flexibility feature of flow batteries. The energy density was raised by using suspensions of energy-dense active materials in a liquid electrolyte. One challenge of this system is the higher pump and component wear due to the suspended particulates in the fluid [48].

Continuous advancements in developing new chemistries and improving existing ones will further improve flow battery efficiency.

2.2.1 Polarization Losses in Batteries

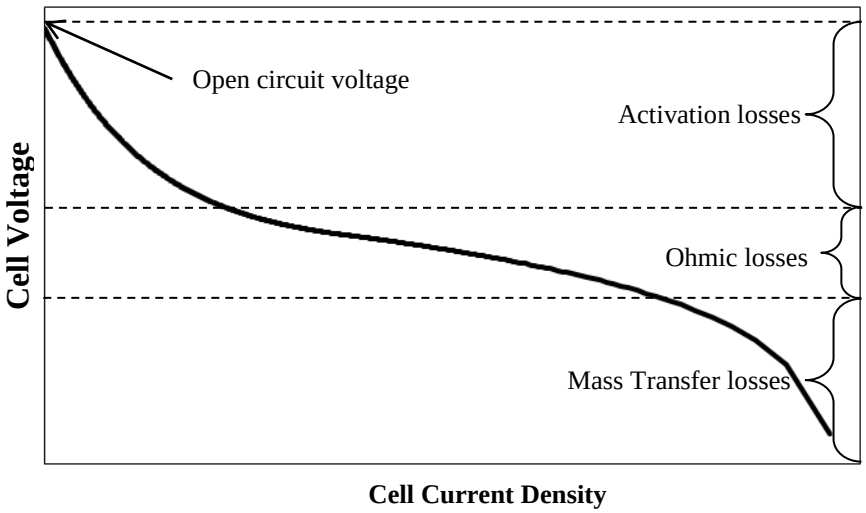

Figure 5: Potential Losses in a RFB [8].

The figure above shows a common polarization curve that demonstrates losses that occur in a typical flow battery set-up. The potential of a cell decreases from its open-circuit value due to irreversible losses in the system resulting from the flow of current. These losses lead to a voltage drop and lower power density. The total cell voltage can be represented as:

Total Cell Voltage = Open Circuit Voltage – Losses

The 3 main factors responsible for the decrease in power density and cell performance are: activation polarization, ohmic polarization and concentration polarization [12], [14], [49]. They are briefly described below:

Activation Overpotential: Activation polarisation is the main cause of cell losses at low operating current densities [8]. It is directly influenced by the rate of the electrochemical reactions and is a result of slow reaction kinetics on the surface of electrodes [50], [51]. An improvement in reaction kinetics achieved by increasing the surface area of electrodes or increasing electrode activity can decrease these losses.

Ohmic Resistance: At intermediate current densities, the internal losses are dominated by ohmic polarization. The resistance to electron and ion transport through the electrodes and electrolyte, respectively, and the contact resistance between various cell components are responsible for ohmic losses [49], [51]. A group from the University of Tennessee decreased the ohmic losses by increasing the compression of the cell components to reduce their contact resistance. They were successful in achieving a high peak power density value of 557MW/cm^2 with the help of their "zero gap" cell [52]. Thinner or more permeable membranes can also assist in improving system performance by reducing the ohmic resistance [8].

Concentration Over-potential: During an electrochemical reaction, the reactant is consumed at the electrode surface. If the supply of the electro-active species to the electrode surface from the bulk electrolyte cannot keep pace with their rate of consumption by the redox reactions during the course of operation, this leads to a concentration gradient and potential drop. The losses due to the depletion of reactants at the electrode are known as concentration polarization [49] and dominate at high current densities [50]. The electrode microstructure, mainly porosity, permeability, tortuosity are the main factors affecting the mass transport of reactants and products through porous electrodes. An improvement in these properties can help minimize mass transport losses and the corresponding voltage drop.

Electrodes are an integral part of a battery. If their structural and transport properties can be improved, then the voltage losses can be reduced and power density improved.

2.3 Porous Media

The electrodes used in RFBs are mostly porous carbon electrodes [53]. A porous medium is defined as a solid body that contains void spaces. Although pores may be interconnected or isolated, they should be interconnected in order for fluid to flow through

them. Some examples of porous media are rocks such as limestone, dolomite, etc., fibrous material such as cloth, felt, carbon paper, electrospun electrodes etc [54]. Images of some porous media are shown below:

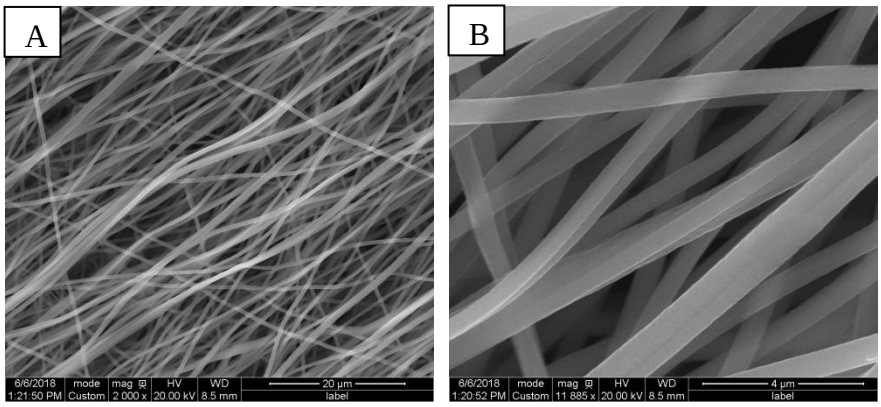

Figure 6: SEM images of PAN nanofibres carbonized at 1500°C for 40 min at A) low and B) high magnification.

Transport phenomena in porous electrodes used in flow batteries are of great importance. As the name implies, the electrolyte in a flow battery is pumped through the cell to reach the surface of the fibrous electrodes. For efficient mass transport within the electrolyte, various physical properties of these electrodes are important: porosity, permeability, tortuosity and electrode thickness. In addition to these properties, the surface area of the electrode should also be taken into account when optimizing the electrode structure. A brief explanation of these properties and their importance for cell performance is given below.

(i) Porosity is defined as the fraction of pore volume to total volume [55]:

$$\in = \frac{V_p}{V_b} = 1 - \frac{V_s}{V_b} \quad (1)$$

where V_p , V_b and V_s are the pore volume, bulk volume and solid volume, respectively.

Commercial flow battery electrodes have a porosity of ~ 75% [9]. High porosity offers several advantages. It ensures enough void space to maintain a sufficient quantity of

electrolyte in the electrode to ensure that continuous reactions occur without depleting the reactant. The amount of current generated is also directly related to the mass or moles of material consumed, as described by Faraday's law of electrolysis [56]:

$$\boldsymbol{n_{electrolyte} = \frac{iA}{nF}} \tag{2}$$

where $n_{electrolyte}$ is the rate of consumption of the reactant, i is current density, A is the area, n is the number of electrons transferred per mole of reactant and F is the Faraday constant.

(ii) Pore size is also an important property to be considered when designing electrodes. Very small pores make it difficult for the electrolyte to flow through. An alternative is to increase the electrolyte flow rate, but doing so will also increase the power consumed by the pump, increase operating costs and lower the system efficiency [57]. The power consumed to pump the electrolyte through the cell is [58]:

$$\boldsymbol{P_{pump} = \frac{Q\Delta P}{\eta_{pump}}} \tag{3}$$

where P_{pump} is the power consumed by the pump, Q is the flow rate, ΔP is the pressure drop and η_{pump} is the efficiency of the pump.

Fibrous electrodes generally have quite large pores and do not face this problem.

(iii)Tortuosity refers to the length of transport pathways in porous electrodes and is strongly dependent on the structural properties of porous media [12], [59]. Since the diffusion path in most porous materials is tortuous, this leads to a reduction in the mass flux [60]. The tortuosity is commonly define as the ratio of the shortest pathway L' through a porous medium to the Euclidean distance L between the starting and end point of that pathway [55], [56], [61], but is sometime given as the square of this ratio.

$$\tau = \frac{L'}{L} \tag{4}$$

Tortuosity is closely related to porosity. A highly porous electrode will have low tortuosity and low porosity will correspond to high tortuosity, as shown in the figure below:

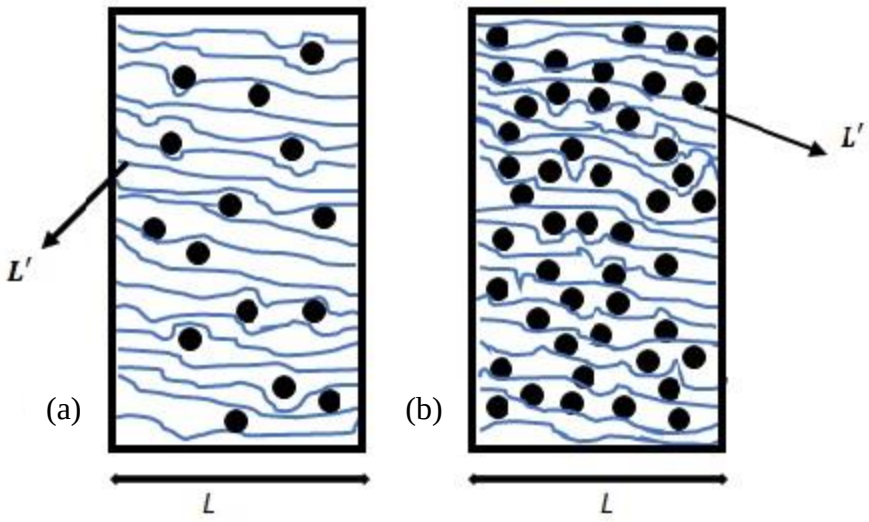

Figure 7: (a) High porosity, low tortuosity. (b) Low porosity, high tortuosity [55].

(iv) Permeability is another important electrode property responsible for mass transfer. It is defined as the resistance offered to convective mass transfer or pressure driven flow as given by Darcy's law:

$$Q = \frac{\kappa A}{\mu L} \Delta P \tag{5}$$

Where Q is the flow rate of the electrolyte, μ is the viscosity of the electrolyte, L is the length across which the pressure drop occurs, A is the cross-sectional area of the electrode and κ is the permeability of the electrode that takes into account the material pore-scale properties such as pore and fibre sizes, porosity, pore connectivity, tortuosity, etc [12], [62]. A low permeability leads to an increase in resistance to flow and thus increases the pressure drop [63] that results in insufficient electrolyte flow through the electrode. Darcy's law stated in equation (5) is valid for incompressible fluids only. If the

fluid used is compressible and flows at a low velocity, then the following form of Darcy's law is applicable:

$$\frac{P_{in}^2 - P_{out}^2}{2LRT/MW_{fluid}} = \frac{\mu}{\kappa} m' \tag{6}$$

where P_{in} is the inlet pressure, P_{out} is the outlet pressure, L is the length of the sample across which pressure drop occurs, R the universal gas constant, T is the temperature, MW_{fluid} the molecular weight of fluid and m' the mass flux through the sample.

For a fibrous material, the permeability κ depends on the fibre diameter d_f and porosityϵ. The relation between all three parameters is given by the Carmen-Kozeny equation [57], [64]:

$$\kappa = \frac{d_f^2 \epsilon^3}{16 k_{ck}(1-\epsilon)^2} \tag{7}$$

k_{ck} is a fitting parameter known as the Carmen-Kozeny constant. The k_{ck} value accounts for the material structure such as fibre morphology and shape. Granular particles have different k_{ck} from fibrous material [62], [65] and aligned fibrous material have different values from randomly aligned fibres [62].

Large fibre diameter and high porosity leads to high permeability according to the Carmen-Kozeny equation but low SA (m^2/m^3) according to the filament analogue model given by equation (8):

$$A_s = \frac{4(1-\epsilon)}{d_f} \tag{8}$$

where A_s is surface area per unit volume of electrode (m^2/m^3). Thus a trade-off is made between better mass transport and kinetics.

(v) Electrode thickness is another important factor. An increase in electrode thickness raises the SA and the number of reaction sites available for the redox reaction. However, this

also increases the distance that ions and electrons must travel and therefore increases ohmic losses.

Thus, we can see that optimizing transport and performance in porous electrodes is not easy since it requires a compromise between various factors.

2.4 Electrospinning

The term electrospinning (ES) is derived from "electrostatic spinning". This technology uses electrical forces to a draw polymer solution into fibres with diameter ranging from 2 nm to several micrometres [66]. Although this technique was first patented by Formhals in 1934, it regained momentum in the early 1990s when Reneker and Chun demonstrated the ease of this technology by electrospinning a wide variety of polymers [67]. Polyamides, polyester, collagen, polypeptides, cellulose acetate and silk protein are examples of some polymer types that have been electrospun [66], [67].

The main components of an electrospinning setup are: a high voltage DC power supply (capable of several tens of kVs), a syringe connected to a needle and a collector (eg., metal plate, rotating drum or disk) for collecting fibres. The power supply is connected either to the collector or to the needle containing the polymer solution. The polymer solution that is held by its surface tension at the tip of the needle experiences mutual electrical repulsive forces acting opposite to its surface tension. As the electric field is increased, the hemispherical drop changes to a conical shape known as a "Taylor" cone. On further increasing the electric field it reaches a critical value at which the repulsive forces overcome the surface tension (cohesive forces) and draw the polymer solution into a fibre that stretches and elongates on its way to the collector while the solvent evaporates [66]–[68]. It is important to use a volatile solvent for electrospinning so that fibres are set in flight before they are collected. Figure 8A shows an image of the Taylor cone formed during electrospinning and Figure 8B represents a basic electrospinning setup.

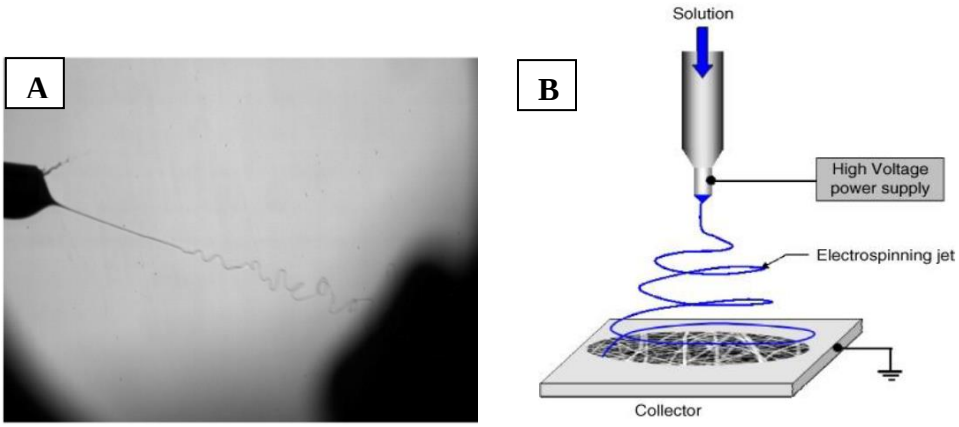

Figure 8: A) Fibre being drawn from tip of Taylor cone during electrospinning. B) Simple electrospinning setup [9].

The various parameters that affect electrospinning are divided into 3 categories: solution parameters (concentration, molecular weight, viscosity, surface tension, conductivity), process parameters (applied voltage, feed rate, needle tip-to-collector distance) and ambient parameters (temperature, humidity). The table below describes the effect of these parameters on fibre formation [66]:

Table 1: Effect of various parameters on electrospinning [66]

Parameters		**Effect on fibre formation**
Solution Parameters:	**Viscosity**	Too low a viscosity leads to bead formation and too high a value will lead to inconsistent electrospinning. Fibre diameter increases with increase in viscosity.
	Polymer Concentration	Too low a concentration leads to a mixture of beads and fibres, whereas too high a concentration prevents continuous electrospinning because of the inability of the solution to flow. An optimum polymer solution concentration is required to obtain uniform fibres. Increasing the solution concentration increases the

		fibre diameter.
	Molecular Weight of Polymer	Increase in molecular weight decreases the number of beads.
	Surface Tension	High surface tension can cause the jet to collapse into droplets before the solvent evaporates.
	Conductivity	Increase in conductivity decreases the fibre diameter.
Process Parameters:	**Applied Voltage**	Fibre diameter decreases with increase in applied voltage.
	Needle tip-to-collector distance	Too small or too high a distance can lead to bead formation.
	Flow Rate	Fibre diameter increases with increase in flow rate, but a very high feed rate can result in a mixture of beads and fibres.
Ambient Parameters:	**Temperature**	Higher temperatures lead to thinner fibres.
	Humidity	High humidity leads to pore formation on fibre surface.

A wide variety of electrospinning techniques such as the use of a single spinneret, coaxial needle, tri-axial electrospinning, emulsion and microfluidic electrospinning have been employed to make unique fibrous structures that find application in various fields [69]. Some interesting morphologies that can be manufactured using this technique include composite core-shell fibres [70], porous fibres [71], tubular or hollow fibre structures [72], helical fibres [73], flat or ribbon-like fibres and aligned fibres. Useful materials that cannot be drawn into fibres by themselves can still be spun into fibres with the help of coaxial electrospinning. For instance, poly(dodecylthiophene) (PDT) is not spinnable by itself, but with the use of

poly(ethylene oxide) (PEO) as a shell polymer and PDT as a core polymer, Zaicheng *et al* were successful in obtaining PDT fibres. The PEO shell simply served as a template [74]. Another example of core shell electrospun structure is silicon nanoparticle-based lithium ion battery anode material obtained by electrospinning polyacrylonitrile solution in the shell and silicon nanoparticles mixed in poly(methyl methacrylate) (PMMA) as the core material. After carbonizing the electrospun fibres, a carbon structure containing Si NPs was formed and ready to be used as a Li-ion battery anode [75].

A hollow fibre or tubular structure is also an interesting morphology that finds application in water filtration, gas separation and dialysis because of the large SA-to-volume ratio. ES is an easy and inexpensive technology that can be used to prepare hollow fibres ranging from nm to micrometre size, unlike the conventional spinning technologies which produce micrometre size fibres [76]. An example of a tubular structure prepared by ES are poly-L-lactic acid (PLLA) hollow fibres obtained by coaxially electrospinning PLLA and polyethylene glycol (PEG) as shell and core material, respectively. PEG was removed from the electrospun core/shell fibre by dissolving it in doubly distilled water to leave behind hollow PLLA fibres. These fibres can be used as scaffolds that mimic original tissues for better regeneration, such as the nerve guide conduits [77].

Porous fibres have also received much attention as they offer high surface area which can be useful in catalysis, batteries, biomedical field, etc. PLLA porous fibres have been produced by electrospinning a solution mixture containing PLLA, its solvent and a non-solvent. These fibres are ideal candidates for drug delivery and tissue engineering because of the large SA offered by their porous structure [78]. Phase separation and breath figures are the two most commonly known mechanisms responsible for the formation of porous fibres [79]–[81].

Flat fibres formed by ES cellulose acetate [82], nylon 11 [83] , polystyrene [84], gelatin [85], silk [86], poly(ether imide) [84], etc have been reported in literature. The change from cylindrical morphology to ribbon or flat fibre morphology has mostly been achieved by changing the electrospinning parameters such as polymer concentration [83]–[85], [87] and molecular weight [87], viscosity of the polymer solution [88], applied voltage [85], ambient temperature [86] or by using a mixture of more highly and less highly volatile solvents [82].

For example, gelatin flat fibres were formed when voltage was increased from 10kV to 25kV [85]. Silk flat fibres were obtained at ambient temperature higher than 25°C [86]. In the case of polysulfone, the use of dichloromethane (DCM) as a solvent instead of n,n-dimethylformamide (DMF) resulted in flat fibres. Since DCM is more volatile than DMF, its rapid vaporization led to skin formation which then collapsed to form flat fibres [89]. Cellulose acetate FFs were formed when the ratio of DCM/acetone was increased. Since DCM is more volatile than acetone, an increase in the ratio of DCM/acetone led to rapid evaporation of the solvent consequently leading to skin formation on the outer surface of the fibre [82]. The formation of flat fibres has most commonly been attributed to rapid vaporization of solvent from the outer surface, leading to skin formation on the outside, while solvent on the inside diffuses through the skin, which then collapses to form FFs [84]. Although many studies have focused on the formation of flat fibre morphology, none of them have been concerned with the use of these flat fibres or investigated the benefits of this morphology relative to that of more conventional cylindrical fibres. In the work presented in this thesis, polyacrylonitrile (PAN) is used as a precursor for fabricating electrodes because of its high carbon yield. Although PAN has been widely used to electrospin cylindrical carbon fibres, flat fibres made of PAN have not been reported, to the best of the author's knowledge. The technique used to make flat fibres is novel, easy and different from those

mentioned in literature. Also, the use of flat fibre electrodes in flow batteries has not been reported to date.

In addition to fabricating novel fibre morphologies, electrospinning can also be harnessed to create macroscopically interesting structures as well. In the present work, the impact of creating highly aligned fibres is also investigated.

Aligned NFs of polymers such as polyurethane [90], polystyrene (PS) [91], poly(lactic-co-glycolic acid) (PLGA) [92], polyacrylonitrile (PAN) [93], [94], nylon 6 [95], gelatin [96] have been reported in the past The easiest way to prepare aligned fibres is by increasing the speed of the rotating collector [90]–[97]. Most research papers focus on the use of aligned fibres in tissue engineering [96] for skeletal muscle repair [92], nerve guide conduits [90], etc. As far as polyacrylonitrile aligned fibres are concerned, researchers have studied their morphology and mechanical strength properties [98]. Attempts have been made to improve their mechanical strength by using MWCNTs[93] and have explored their use in air filtration [94]. However, little attention has been paid to characterizing their transport properties [62] and exploring their potential for use as electrodes in RFBs.

Conductive nanofibrous membranes are finding great use as porous electrodes in developing high performance batteries (eg., lithium-ion) and polymer electrolyte membrane fuel cells (PEMFCs) due to their high porosity and large surface area achieved by small fibre size [66]. However, less attention has been given to use of conductive electrospun mats in flow batteries [9].

2.5 Carbonization

Carbonization transforms non-conductive electrospun fibrous mat into conductive electrodes. Carbon fibres can be produced from a variety of precursors but almost 90% of the global carbon fibre production is PAN based [99]–[102]. The 68% carbon content in homopolymer PAN exceeds 90% in the final carbon fibre formed after heat treatment. As the

carbonization temperature is increased, the carbon fibre modulus increases and the carbon content continues to increase [102]. The molecular structure of PAN $[C_3H_3N]_n$ is shown below:

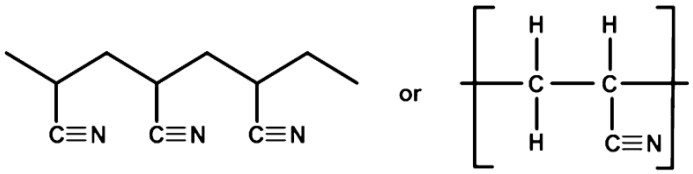

Figure 9: Molecular structure of polyacrylonitrile(PAN) [103].

The 3 main stages involved in the carbonization of PAN-based fibres are [100]:

(i) Stabilization in an oxidizing medium (usually air) at temperature between 180°C and 300°C.

(ii) Carbonization in an inert condition (usually nitrogen) to keep out the non-carbon atoms ≤ 1600°C.

(iii) Graphitization (further heating the fibre to 2000°C - 3000°C) to increase stiffness of the fibre.

Stabilization is the most time-consuming and crucial step in the heat treatment process for converting PAN based fibres into carbon fibres. Several important reactions such as cyclization, dehydrogenation and oxidation take place in this stage [101]. In the stabilization process, a linear polymer is converted into a heterocyclic six-membered ring ladder structure which makes the fibrous material rigid and capable of withstanding high temperatures in the subsequent stages. The primary goal of stabilization is to inhibit the melting or fusion of the fibre and to avoid excessive volatization of elemental carbon at the higher temperatures in the following carbonization step in order to maximize the ultimate carbon yield from the fibre precursor. Upon cyclization, the fibre changes color from white to shades of yellow or dark brown to eventually black as it is stabilized. To fabricate carbon fibres possessing good

mechanical strength, it is extremely important to ensure completion of the stabilization reactions [100]. Another important factor to consider is the temperature for this stage. If the temperature is too low, the reactions are slow and will be incomplete, yielding poor carbon fibre properties [103]. If the stabilization temperature is too high, then the fibre can become overheated and fuse together or may even burn [104].

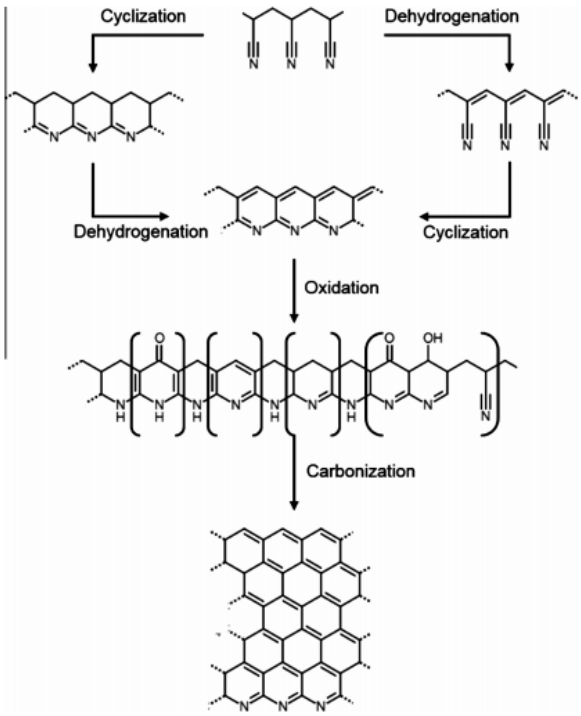

Figure 10: Chemical conversions that occur during stabilization and carbonization of PAN [102].

The carbonization process is carried out in an inert atmosphere in the temperature range 1000°C-1600°C. In this stage, the stabilized ladder structure transforms into a more well-ordered structure. Non-carbon elements are released thereby increasing the carbon content. As the temperature is increased, the carbon content rises even further and so do the carbon fibre tensile strength and modulus [102], [103]. Graphitization involves heat treatment of the sample at a much higher temperature of ~ 3000°C that results in the conversion of carbon structure into graphite. Carbon fibre produced in this step has a very high modulus [103].

3 Experimental Techniques

A custom-built setup was used to electrospin polymer solutions using a single nozzle needle or coaxial needle to form a fibrous mat. After electrospinning, the fibrous mat was carefully peeled off from the aluminium foil and observed under SEM. This section includes the chemicals used, material production method and description of the various characterization techniques used to determine the structural and transport properties of the electrodes.

3.1 Chemicals

The chemicals used include polyacrylonitrile (PAN) (average MW 150,000), polystyrene (PS) (average MW 280,000), N,N-dimethylformamide (DMF) (99.8%), chloroform (99.8%) and pentane (99.8%). All chemicals were purchased from Sigma Aldrich and used directly without further purification.

3.2 Material Production

The electrospinning technique was used to produce both flat fibres and aligned fibres.

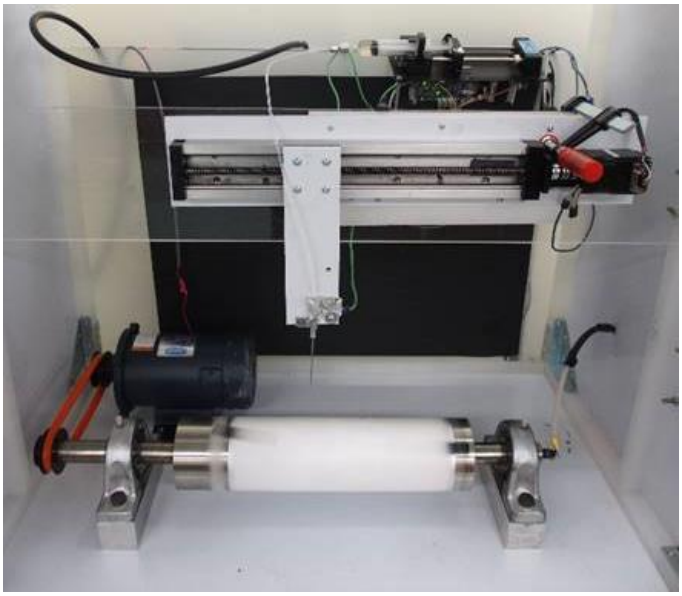

Figure 11: Electrospinning setup used in this study.

3.2.1 Electrospinning Flat Fibres

Various electrospinning approaches were investigated to make flat fibres. The sections under this topic describe all the methods that were employed to make flat fibres. Each section provides details regarding the polymer solution preparation, electrospinning set-up and conditions used to make flat fibres. Many of these techniques did not work, but are listed here to provide a comprehensive overview as a reference point for future studies.

3.2.1.1 Coaxial Electrospinning: PAN/DMF (shell & core)

PAN was dissolved in DMF to prepare 12 wt% and 2 wt% PAN/DMF solutions for use in shell and core of the coaxial needle, respectively. The solutions were stirred for 20 h without heating to avoid thermal degradation and ensure homogeneity. The custom-built electrospinning set-up consisted of a coaxial needle, two syringe pumps, linear motion actuator, rotating drum with 10 cm (4 inch) diameter and a high voltage power supply (Glassman, MJ30N0400-11). Syringes loaded with polymer solution were connected to a coaxial needle via a tube. All samples were spun using a coaxial needle of size 11 g / 14 g (shell/core size). Different flow rate combinations of shell and core solution were tried. The shell solution and core solution flow rates were varied from 1.0 to 1.4 ml/hr and 0.5 to 1.2 ml/hr, respectively, at increments of 0.1 ml/hr. Each possible treatment combination of the shell and core solution flow rate was tried. A distance of approximately 11 cm was maintained between the needle tip and the collector. During electrospinning, a negative voltage of 15 kV was supplied to the collector while all other components including the needle were grounded. Charging the drum collector instead of the needle helped to stabilize the electrospinning process. The speed of drum measured with a tachometer was maintained at 5 m/min. The rotating drum was covered with aluminium foil to collect the fibres. After electrospinning, the fibres were carefully peeled from the aluminium foil for SEM imaging.

3.2.1.2 Use of Heat Gun

The polymer solutions used for the shell and core of the coaxial needle were prepared by dissolving PAN in DMF. 14 and 12 wt% solutions were prepared for the shell of the needle and 2 wt% solution was prepared for core. The solutions were stirred for 20 h without heating to avoid thermal degradation and ensure homogeneity. The set-up described in section 3.2.1.1 was used for this experiment. For the 14 wt% shell / 2 wt% core combination, the shell and core solution flow rates were maintained at 1.2 ml/hr and 1.0 ml/hr, respectively. In the case of the 12 wt% shell / 2 wt% core combination, the shell and core solution flow rates were maintained at 1.0 ml/hr and 0.8 ml/hr, respectively. The distance between the needle and collector was 11 cm and a negative voltage of 15.0-18.0 kV was applied to the drum. During electrospinning, a heat gun was used to raise the temperature of the fibre surroundings to promote rapid evaporation of the solvent.

3.2.1.3 PAN/Nitric Acid

A 12 wt% polymer solution was prepared by dissolving PAN in nitric acid. The solution was stirred for 20 h without heating to avoid thermal degradation and ensure homogeneity. The set-up used was the same as described in section 3.2.1.1 except that a single nozzle needle of size 16 gauge was used. A distance of 11 cm was maintained between the needle and collector. A negative voltage in the range of 12.0-18.0 kV was applied to the collector. The solution flow rate was varied from 0.5-1.0 ml/hr.

3.2.1.4 Polystyrene/DMF

A 30 wt% polymer solution was prepared by dissolving polystyrene (PS) in DMF. The solution was stirred for 24 h without heating to avoid thermal degradation and ensure homogeneity. The setup described in section 3.2.1.1 was employed for this method. This experiment was done to replicate the method used by Koombhongse *et al* [84] to form polystyrene flat fibres. With the exception of the needle size, all other conditions used were

the same as that described in their research paper. A comparison of the parameters used is given below in Table 2:

Table 2: Electrospinning Parameters

Factors	**Koombhongse**	**This study**
Polymer Concentration	30 wt%	30 wt%
Distance	20 cm	20 cm
Voltage	20 kV	16, 18, 20 and 24 kV
Polarity	Not mentioned.	Used both negative and positive power supply.
Connect the power supply to needle or collector	Charged the needle.	Charged the needle. Also conducted experiment by charging the collector.
Flow Rate	Hydrostatic pressure with a liquid column of height 1-2 cm.	Hydrostatic pressure with a liquid column of height 1-2 cm.
Needle Size	0.3 mm	16 g (1.29 mm)
Temperature	Not mentioned.	Room temperature (22℃).

3.2.1.5 Coaxial Electrospinning: PAN/DMF (shell) and Pentane (core)

A 12 wt% polymer solution was prepared by dissolving PAN in DMF. The solution was stirred for 20 h without heating to avoid thermal degradation and ensure homogeneity. The set-up used was the same as mentioned in section 3.1.1.1. The 12 wt% PAN/DMF solution was supplied to the shell and pure pentane was delivered to the core of the needle. A distance of 11 cm was maintained between the needle and collector. The solution was electrospun at various negative voltages applied to the collector: 9, 12, 15 and 18 kV. The shell solution and core solution flow rates were varied between 0.8-1.4 ml/hr and 0.5-1.2 ml/hr, respectively.

3.2.1.6 Coaxial Electrospinning: PAN/DMF (shell) and PS/$CHCl_3$ (core)

The polymer solution used in the shell and core of the coaxial needle were prepared by dissolving PAN in DMF and PS in chloroform, respectively. 12 wt% and 22 wt% solutions were prepared for the shell and core, respectively. The solutions were stirred for 24 h without heating to avoid thermal degradation and ensure homogeneity. The set-up used was same as mentioned in section 3.2.1.1.

3.2.1.7 Coaxial Electrospinning: PAN/DMF (shell) and PS/DMF (core)

The polymer solutions used in the shell and core of the coaxial needle were prepared by dissolving PAN in DMF and PS in DMF, respectively. All possible combinations of shell solution (denoted SS) concentration: 9, 12 and 13.5 wt% were coupled with core solution (denoted CS) concentrations of 30, 33 and 35 wt%. The solutions were stirred for 20 h without heating to avoid thermal degradation and ensure homogeneity. Concentration plays a crucial role in electrospinning. A low concentration polymer solution can lead to bead formation instead of uniform fibres whereas a very high concentration can make electrospinning difficult because of the excessive viscosity. Based on this, the lower and upper limit of concentration were selected for both PAN/DMF and PS/DMF solutions. The flow rates for both shell and core solution were maintained at 1.0 ml/hr using a syringe pump. The flow rate of the solutions was decreased over time to ensure steady electrospinning, while still maintaining a SS:CS flow rate ratio of 1:1. A coaxial needle of size 11 g / 14 g (shell/core) was used. A distance of about 9 cm was maintained between needle and collector. During electrospinning, a negative voltage of 15 kV was supplied to the collector while all other components including the needle were grounded. After electrospinning, the fibres were carefully peeled off from the aluminium foil and cut into pieces of size 10 cm x 10 cm. The fibrous mat was then dipped in chloroform to extract polystyrene from the core of the composite fibre. This resulted in a hollow core which was unable to support the thin shell and

thus caused it to collapse to form flat fibres. After extraction, the mat was removed from chloroform and dried at room temperature in a fumehood. Care was taken to prevent the wet fibrous mat from sticking to the aluminium foil by flipping it after every 2-3 minutes.

3.2.2 Electrospinning Aligned Fibres

A 12 wt% polymer solution was prepared by dissolving PAN in DMF. It was allowed to mix for 20 h without heating to avoid thermal degradation and ensure homogeneity. The solution was electrospun using a 16 gauge needle kept at a distance of 12 cm from the collector. A negative voltage of 15 kV was applied to the collector (a rotating drum). To collect aligned fibres instead of random fibres, the speed of the rotating drum was set to a high value of 10 m/sec. The flow rate of solution was set at 0.45 ml/hr in the beginning and then decreased as the thickness of the fibrous mat increased. This procedure was adopted because the fibrous mat is non-conductive which causes the strength of electric field across it to decrease as it accumulates. Without a decrease in solution flow rate, this caused the solution to drip from the needle tip rather than form a continuous stream.

3.2.3 Carbonization of Fibres

The electrospun fibres were carbonized in a tube furnace. Samples with size 9 cm x 5 cm were cut and placed between two alumina plates that were approximately 0.425 cm thick. These plates were essential to ensure a flat and compact electrode. Stainless steel shims that were slightly thinner than the mat were placed between the plates near the edges to prevent extreme compression of the sample. The procedure for carbonization of PAN fibres is well described in the literature [17]. It involved heating at a constant rate of 5ºC/min. The sample was stabilized in air by heating it from room temperature to 250ºC and then holding it at 250ºC for 3 h. After the sample had been stabilized for two hours and 45 min, nitrogen was introduced at a flow rate of 200 sccm. Once the stabilization process was complete, the

temperature was increased to 850ºC and maintained at this temperature for 40 min followed by heating to 1050ºC and holding it at this temperature for another 40 min. The furnace was then cooled at a rate of 5ºC/min to 250ºC and then allowed to cool to room temperature. The sample was heated again to a temperature of 1500ºC at a rate of 5ºC/min. This was done to increase the carbon content and stiffness of the sample [100].

Figure 12: Tube Furnace used for carbonization.

3.3 Characterization Methods

3.3.1 SEM Characterization

The samples were observed using scanning electron microscopy (Quanta FEG 250) to determine the fibre shape, size and general morphology. The images obtained were further analyzed to estimate the fibre diameter of cylindrical fibres and fibre width of flat fibres using ImageJ software. Line segments were drawn across the fibres and the length of the segment was taken to be the diameter of cylindrical fibres (d_f) and width of flat fibres (w_f). Samples were taken from 5 different locations on the mat and approximately 5-10 measurements were taken of each image to obtain the average value of d_f/w_f and standard deviation.

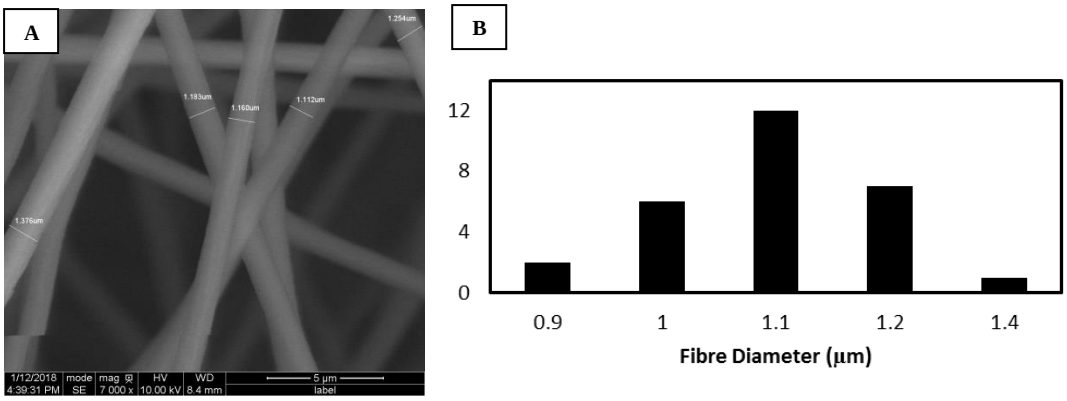

Figure 13: A) Line segments drawn to measure fibre diameter. B) A histogram representing fibre diameter on x-axis.

3.3.2 Porosity Measurement

The buoyancy method is an easy, non-destructive, fast and highly reproducible method to determine the porosity of thin fibrous materials such as PEMFC gas diffusion layers[16]. The porosities of both uncarbonized and carbonized samples were obtained using this method. A sample was obtained by cutting a circular disc of diameter 7/8 inch. Thickness of the sample was measured using a micrometer with 1 µm resolution and ± 0.1 µm accuracy equipped with a thumb clutch. The sample was then weighed both dry and submerged in a highly wetting fluid such as silicone oil. Using the Archimedes principle, the solid or skeletal density was determined as:

$$\boldsymbol{\rho_s = \rho_l \frac{m_{s,a}}{m_l} = \rho_l \frac{m_{s,a}}{m_{s,a} - m_{s,l}}} \tag{9}$$

where ρ_s is the solid density, ρ_l is the liquid density, m_l is the mass of the liquid displaced and $m_{s,a}$ and $m_{s,l}$are the mass of the solid in air and liquid, respectively.

The solid volume and porosity were then calculated using equations (10) and (11), respectively.

$$\boldsymbol{V_s = \frac{m_{s,a}}{\rho_s}} \tag{10}$$

$$\in = 1 - \frac{V_s}{V_b} \tag{11}$$

where V_s is the solid volume and $\in$ is the porosity of the sample.

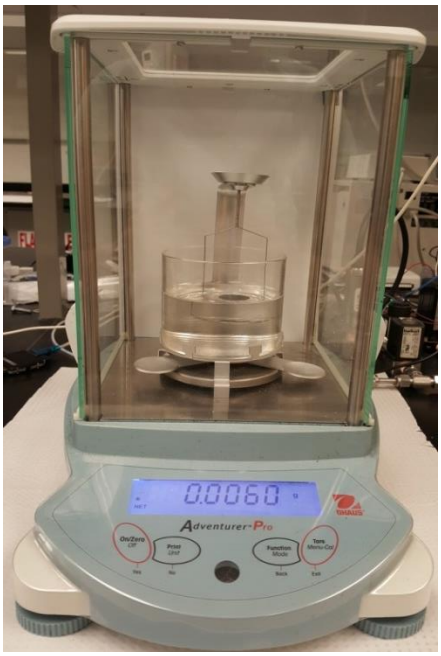

Figure 14: Porosity measurement set-up used in this study.

3.3.3 Permeability

The in-plane permeability of the electrospun and carbonized materials was measured using a device developed by Gostick *et al* [105] and adapted for electrospun material by Kok *et al* [62] and Liu *et al* [17]. Compressed nitrogen gas was supplied at the inlet. Its flow rate was controlled using a mass flow controller (MKS 1160B Series) with a range of 0 to 200 sccm. Since the fluid used for permeability measurement was compressible (i.e. nitrogen), the following form of Darcy's Law was used:

$$\frac{P_{in}^2 - P_{out}^2}{2LRT/MW_{N_2}} = \frac{\mu}{\kappa} m' \tag{12}$$

where P_{in} is the inlet pressure, P_{out} is the outlet pressure, L is the length of the sample, R is the universal gas constant, T is the temperature, MW_{N2} the molecular weight of nitrogen and m' is the mass flux through the sample.

Since the flow rate did not exceed 200 sccm, the Forchheimer effect was not observed [105]. The pressure at the inlet was measured using a pressure sensor (Omega PX409-030A5V, 0 –30 psia range) and the outlet pressure was open to atmosphere and confirmed by a local weather station. A 0.5″ × 2″ sample was cut and placed in the sample holder. The permeability was measured at varying degrees of compression controlled by placing shims of known thickness between the plates prior to tightening them together.

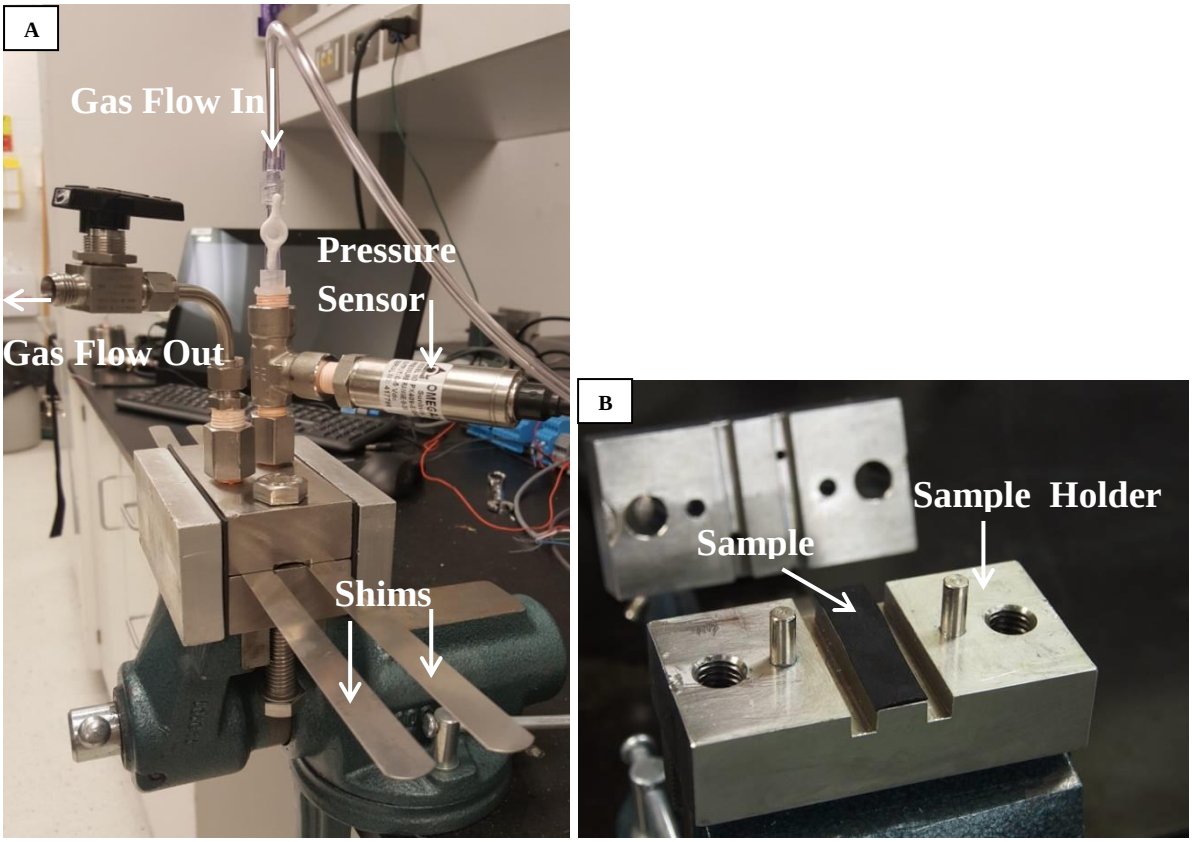

Figure 15: A) Permeability setup used in this study B) Sample placed on sample holder.

3.3.4 Electrical Conductivity

In-plane electrical conductivity was measured using the Van der Pauw method. A custom-made sample holder shown in Figure 16 was used for this method. A sample of size 1.3″ × 1.3″ was placed on the top of the base. Four copper strips were then placed on top of the 4 corners of the sample, acting as the four conductive contact points. A circular ring was placed on top of the copper strips and bolted to the sample holder base to ensure good contact

between the copper strips and the sample. A power supply was used to supply current along one edge (for example between point 1 and 2), while a voltmeter was connected to points 3 and 4 to measure the voltage drop. The resistivity was calculated with the following relationship:

$$\boldsymbol{R_{12,34} = \frac{V_{34}}{I_{12}}} \tag{13}$$

where $R_{12,34}$ is the resistivity, V_{34} is the voltage drop measured between points 3 and 4, I_{12} is the current applied between points 1 and 2. The measurement was repeated for the other direction, i.e., current was applied between points 2 and 3 and voltage drop was measured between terminals 4 and 1. The sheet resistance, R_s, was calculated by finding the value of R_s that satisfies this following equation:

$$\boldsymbol{e^{-\frac{\pi R_{12,34}}{R_s}} + e^{-\frac{\pi R_{23,41}}{R_s}} = 1} \tag{14}$$

where $R_{12,34}$ and $R_{23,41}$ are the resistivities measured with two different configurations. The bulk conductivity σ_{bulk} can then be determined using:

$$\boldsymbol{\sigma_{bulk} = \frac{1}{R_s t}} \tag{15}$$

where t is the average thickness of the sample.

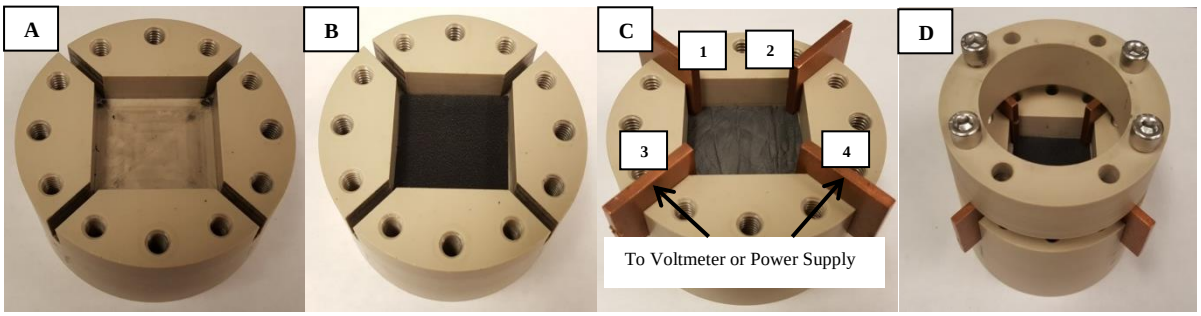

Figure 16: Electrical conductivity setup: A) sample holder base B) sample placed on sample holder base C) copper strips placed on 4 corners of the sample and D) assembled setup.

3.3.5 Surface Area

The specific surface area (m^2/g) of the samples was measured using vapor sorption analysis carried out with a DVS Resolution device from Surface Measurement Systems. The adsorbate used was ethanol. The sample was cut into pieces of size $1cm \times 1cm$ and degassed by pre-heating it to a temperature 100ºC before starting the surface area measurement. Samples with mass of 10-20 mg were used to obtain reliable results. The surface area value was obtained from the isotherms using the commonly used Brunauer-Emmett-Teller (BET) theory. The BET equation used is:

$$\frac{P/P_o}{V_{ad}\left(1 - P/P_o\right)} = \frac{C-1}{CV_{ad,mon}}\left(P/P_o\right) + \frac{1}{CV_{ad,mon}} \tag{16}$$

where P and P_o are the equilibrium and saturation pressure of adsorbate at the temperature of adsorption, C is the BET constant, V_{ad} is the volume of the adsorbate and $V_{ad,mon}$ is the monolayer volume of the adsorbate which can be calculated to yield the sample surface area.

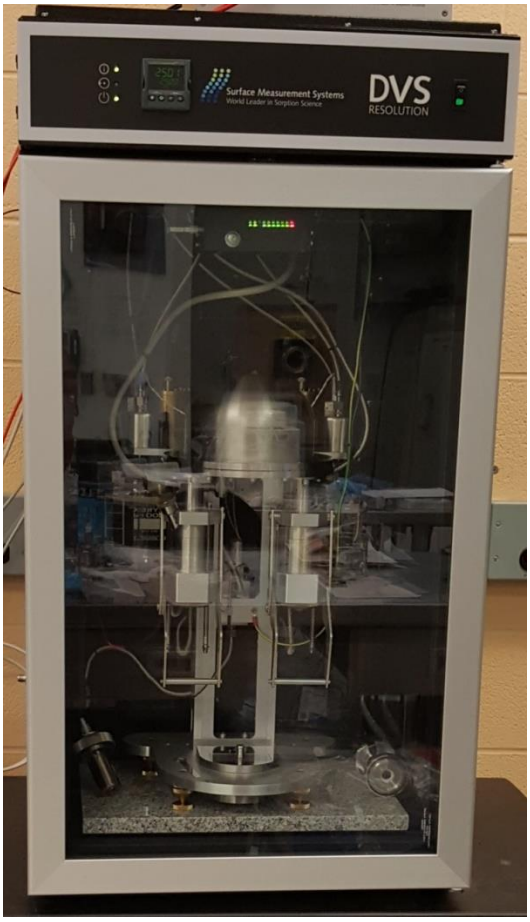

Figure 17: DVS Resolution device for SA analysis used in this study.

3.4 Flow Battery Validation

Characterization of the flat fibre electrodes helped in gaining an understanding of their structural and transport properties. To test their feasibility, the flat fibre electrodes were tested in an all-vanadium flow battery and compared to off-the-shelf material (Freudenberg), as a performance baseline.

3.4.1 Electrolytes

Sulphuric acid (Sigma Aldrich, 95.0-98.0%) and vanadyl sulfate hydrate (Alfa Aesar, 99.9% metals basis) were purchased and used without further purification. Thermogravimetric analysis (TA instruments SDT Q600) was carried out to determine the water content in vanadyl sulfate hydrate. Approximately 15 mg of sample was taken in an

alumina pan and heated in a nitrogen atmosphere at a rate of 10°C/min to a final temperature of 105°C and then heated isothermally for 2 h. The mass lost by the sample was taken as the water content and was accounted for in the preparation of stock solutions of the electrolyte.

3.4.2 Flow Cell Assembly

A 2.55 cm^2 flow cell was used in this study that has also been reported previously [106], [107]. Backing plates were made of propylene. Inter-digitated flow fields with 7 channels (1 mm wide × 0.5 mm deep; 3 outlets and 4 inlets), were machined from 3.18 mm thick impregnated graphite (G347B graphite, MWI, Inc.). Flat fibre electrodes were tested in the flow cell prior to testing the commercial Freudenberg electrode. Two layers of Freudenberg were used to maintain a comparable electrode thickness (ca. 300 μm) to the flat fibre electrodes. Each electrode was cut to a size of 1.4 cm × 1.6 cm to seal it within the open gasket area (1.5 cm × 1.7 cm). The PTFE gaskets were selected to be 75-80% of the uncompressed electrode thickness such that during operation, electrode compression was 20-25%. The membrane, Nafion® NR-212 (Nafion Store, Ion Power) was soaked in 2.6 M $H2SO_4$ for more than 24 h prior to use. Glass scintillation vials with a rubber septa lid were used as electrolyte reservoirs. The septa allowed for inlet and outlet electrolyte tubes along with a 1/16" PTFE tube for continuous nitrogen flow and a 21 ga. needle for venting it. Nitrogen flow was important to prevent capacity fade in the presence of oxygen. The electrolyte flowrate was regulated with the help of a peristaltic pump (MasterFlex) with an Easy-Load II pump drive (Cole-Parmer). Masterflex® Norprene tubing L/S 14 (ID 1.6 mm, OD 4.8 mm, Cole-Parmer) was used to connect the flow cell, pump head and electrolyte reservoirs via barbed fittings.

3.4.3 Flow Cell Testing

All electrochemical experiments were conducted at room temperature using an Arbin Battery Tester (FBTS, Arbin Instruments) for electrolytic preparation and polarization analyses. Oxygen was removed from electrolyte reservoirs by continuously bubbling nitrogen gas (Airgas, 99.999%) through them. A fixed electrolyte flow rate of 10 mL/min was used for all experiments. The V^{2+}/V^{3+} electrolyte was prepared by electrolysis in a flow cell as reported in previous literature [108]. In the initial set-up stage, 30 mL mixture of 1.5 M $VOSO_4$ and 2.6 M H_2SO_4 was used on the negative side and 30 mL of the same electrolyte was used on the positive side. The cell was charged via a potentiostatic hold at a cell voltage of 1.7 V, until the current density decayed to less than 4 mA/cm^2. This step oxidized the V^{4+} to V^{5+} on the positive side and reduced the V^{4+} to V^{3+} on the negative side. After charging, the V^{5+} reservoir was replaced with 30 mL of 1.5 M $VOSO_4$ and 2.6 M H_2SO_4. Once the initial electrolyte charging process was complete, the cell was then discharged to 0.6 V at 100 mA/cm^2 and was then recharged at the same current density, for half of the previous discharge time to reach 50% state-of-charge (SOC). The cell power performance was determined using galvanostatic polarization which was performed with a 30 s hold per step. This allowed the cell to attain a steady state potential. A potential limitations of 0.6 – 1.7 V was used for polarization and the last 50% of the data points at each step were averaged to obtain steady state current and potential values. Polarization accuracy was maintained by recharging the cell at 25 mA/cm^2 between each discharge step back to 50% SOC.

4 Development and Analysis of Flat Fibre Electrodes

This chapter describes the various strategies that were used to make flat fibres and provides detailed analysis of flat fibre properties.

4.1 Fabrication of Flat Fibres

This section discusses the attempts to make flat fibres. Each sub-section explains the motivation for the particular approach used, presents the result obtained and discusses the reason for its failure or success.

4.1.1 Coaxial Electrospinning: PAN/DMF (shell and core)

As mentioned in section 3.2.1.1, 12 wt% and 2 wt% PAN/DMF solutions were supplied to the shell and core of the coaxial needle, respectively. Since the SS was of higher concentration than the CS, the amount of solvent present in the SS was less than that in the CS. Thus, during electrospinning, it was expected that the small amount of solvent in the fibre shell would evaporate away leading to a solid shell, while the excess solvent from the fibres core would diffuse out slowly and leave behind a less dense core. The atmospheric pressure would then cause the shell to collapse and form flat fibres. However, SEM images showed only cylindrical fibres.

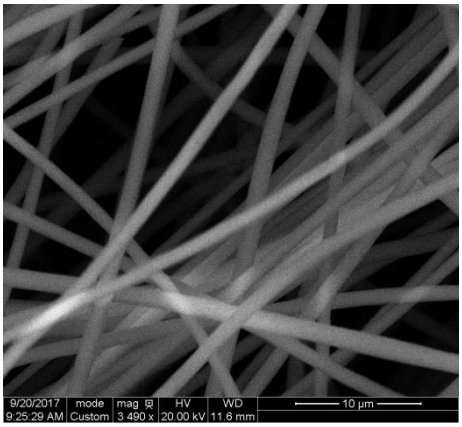

Figure 18: Cylindrical fibres obtained at SS and CS flow rates of 1 ml/hr and 0.8 ml/hr, respectively.

The reason for cylindrical fibre formation could be that DMF is not highly volatile. Some of the solvents such as DCM that have been used to form flat fibres [89] are much more volatile than DMF. It is possible that DMF did not evaporate fast enough from the shell, while the shell and core solutions mixed together to form a homogeneous solution that produced cylindrical fibres. Another possible reason is that the void space formed in the core as the solvent evaporated was immediately occupied by the polymer in the shell so hollow core was not produced.

4.1.2 Use of Heat Gun

Since DMF is not highly volatile, a heat gun was used to increase the temperature of fibre surroundings to promote rapid evaporation of DMF from the outside surface. However, this approach did not yield flat fibres in the two cases when 12 wt% / 2 wt% (shell/core) and 14 wt% / 2wt% (shell/core) PAN/DMF solutions were electrospun, as shown in the SEM images below.

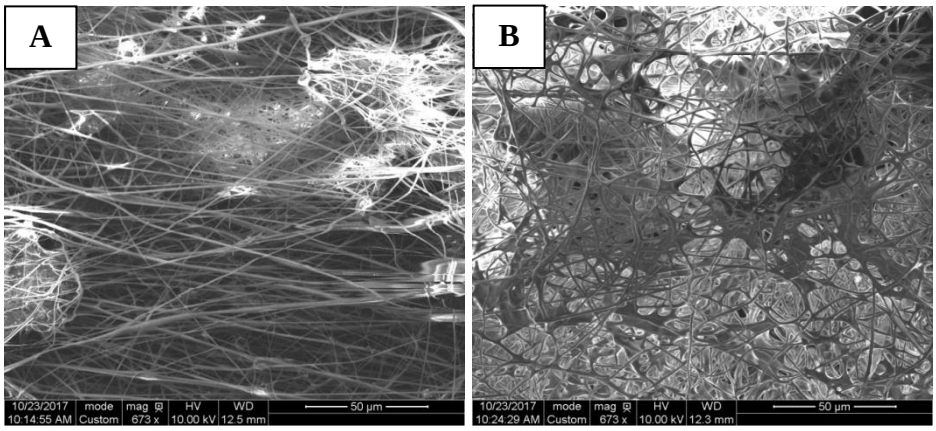

Figure 19: Fibres formed by electrospinning from: A) 12 wt% / 2 wt% shell/core and B) 14 wt% / 2 wt% shell/core solutions.

It is possible that since the same components were present in the polymer solutions (though at different concentrations) in the shell and core of the needle, they may have mixed in the drop formed at the needle tip to form a homogeneous solution that led to cylindrical fibres. It is also possible that the void space created in the core as the solvent evaporated was

simultaneously occupied by the polymer in the shell and as a result no hollow core was formed at all, thus resulting in the formation of cylindrical fibres.

4.1.3 PAN/Nitric Acid

In the literature, a few researchers obtained flat fibres when they replaced a less volatile solvent such as DMF with a more volatile solvent such as DCM. The highly volatile solvent evaporated much faster than a less volatile solvent, thus leading to skin formation on the outside surface of the fibre which then collapsed to form flat fibres [89]. For the same reason, nitric acid was used as a solvent since it is more volatile than DMF. The disadvantage of PAN is that it is only soluble in a limited number of solvents which are less volatile than those used to make flat fibres composed of polymers polysulfone [89], cellulose acetate [82], etc. This made the formation of flat fibres even more challenging. The two most volatile solvents for PAN are nitromethane and nitric acid. Nitromethane is carcinogenic and therefore avoided. Although PAN dissolved and formed a homogenous solution in nitric acid, the solution did not spin at all.

4.1.4 Polystyrene/DMF

The methodology to make PS flat fibres was adopted from Koombhongse *et al* [84] in order to confirm if the technique and conditions that they described in their paper actually lead to flat fibres or not. Apart from the needle size, all other conditions used were the same as in their paper. However, the SEM images for fibres spun under the various conditions showed only cylindrical fibres, as shown below.

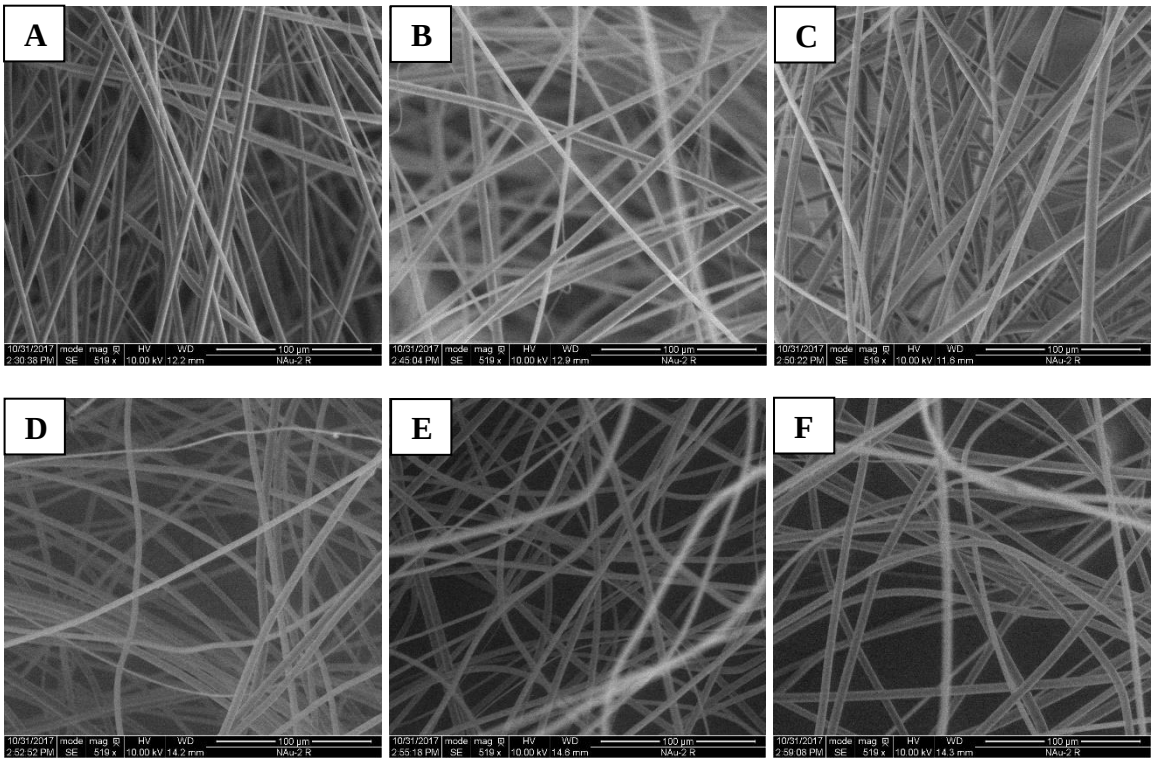

Figure 20: Fibres formed with needle charged to: A) +16, B) +20, C) +24, D) -16, E) -20 and F) -24 kV.

Koombhongse *et al* claimed that rapid evaporation of solvent leads to skin formation on the outside surface of the fibre that then collapses to form flat fibres. Since DMF is not highly volatile, it is possible that Koombhongse *et al* used some technique to promote fast evaporation of DMF but did not describe it in their paper.

4.1.5 Coaxial Electrospinning: PAN/DMF (shell) and Pentane (core)

As explained in sections 4.1.1 and 4.1.2, it is possible that that the core and shell solution mixed together to form a homogeneous solution which prevented hollow cores and cylindrical fibres from forming. In order to avoid this, two immiscible solvents were used in the shell and core of the needle. Both PAN and DMF are immiscible in pentane and thus this would avoid mixing of the shell and core solutions. Another reason for using pentane was that it is highly volatile. This would allow the solvent from the core to diffuse through the shell and evaporate rapidly leaving behind a hollow core. The shell would then collapse and

form flat fibres. However, once again, only cylindrical fibres were observed in the SEM images (Figure 21).

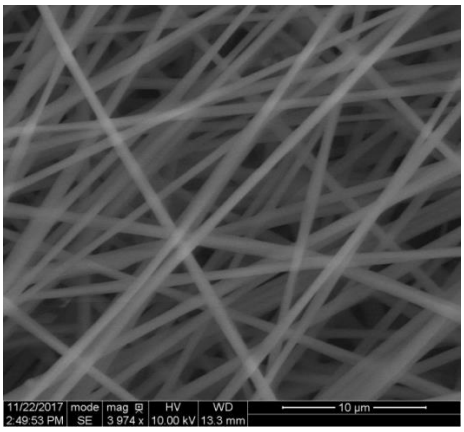

Figure 21: Fibres formed on using PAN/DMF as SS and pentane in core of the needle.

During electrospinning, two streams were observed to leave from the drop tip. The outer stream was electrospinning a thin fibre, while the other stream was electrospraying. The PAN/DMF solution on the outside appeared to be drawn into the cylindrical fibre which can be seen in the figure above whereas the pure pentane was electrospraying. For a solution to electrospin, its concentration should exceed a critical value; otherwise, electrospraying occurs. The pure pentane used in the core was unable to remain in the core of the droplet formed at the needle tip because of its poor viscosity and therefore started electrospraying instead of remaining in the fibre core. Thus, this approach failed and led to formation of cylindrical fibres.

4.1.6 Coaxial Electrospinning: PAN/DMF (shell) and PS/$CHCl_3$ (core)

In the approach discussed above in section 4.1.5, both electrospinning and electrospraying were observed. Electrospraying of pentane occurred because it could not remain in the core due to its low viscosity. Thus, the next step was to use a polymer solution that had a higher viscosity for electrospinning by dissolving a polymer in pentane. After electrospinning, the polymer in the core could be extracted by dipping the fibrous mat in pentane. The shell would then collapse to form flat fibres. Due to the unavailability of a

pentane soluble polymer, a polystyrene/chloroform solution was used in the core of the coaxial needle. Chloroform was used as a solvent since it does not dissolve PAN and thus would prevent PAN from mixing with the core solution and force it to remain in the fibre shell. However, during electrospinning, the solution did not spin because the drop formed at the needle tip became gel-like and very viscous. Being highly volatile, might have diffused out from the core into the shell and finally evaporate. Its diffusion into the shell may have caused PAN to precipitate out and form a gel-like drop which prevented electrospinning.

4.1.7 Coaxial Electrospinning: PAN/DMF (shell) and PS/DMF (core)

To improve on the approach used in section 4.1.6, a PS/DMF solution was used in the core of the needle and PAN/DMF in the shell. After electrospinning, the fibrous mat was dipped in chloroform to extract polystyrene from the fibre resulting in a hollow core. The shell then collapsed to form flat fibres. The success of this idea also demonstrated that the likelihood of the shell and core solution being mixed completely are slim because electrospinning is more rapid than diffusion. Thus, before the SS and CS form a homogeneous solution due to diffusion, the solvent evaporates to form a solid fibre during electrospinning.

Various concentrations of shell and core solution were then electrospun to determine the concentration combination at which maximum flat fibres could be produced in a minimum time frame. The shell solution (PAN/DMF) concentrations used were 9, 12 and 13.5 wt%, while the core solution (PS/DMF) concentrations used were 30, 33 and 35 wt%. Experiments were conducted in a random order and were replicated to select the appropriate shell and core solution concentration combination. The table below gives the width of the flat fibres obtained in each case:

Table 3: Width of flat fibres for different SS and CS concentrations

PS/DMF / PAN/DMF	30 wt%	33 wt%	35 wt%
9 wt%	1.5 ± 0.1 µm	1.9 ± 0.3 µm	2.0 ± 0.2 µm
12 wt%	2.0 ± 0.1 µm	2.4 ± 0.1 µm	2.4 ± 0.2 µm
13.5 wt%	2.2 ± 0.1 µm	2.4 ± 0.2 µm	2.5 ± 0.3 µm

It was observed that the fibre width increased with increasing concentration of SS or CS or both. With an increase in concentration, the fibre diameter increases [109], [110] and produces wider flat fibres upon collapse.

Although flat fibres were obtained for each combination mentioned above, the time required to extract polystyrene from the fibre core was different for each treatment. The figure below shows SEM images of mats spun at a fixed SS concentration of 9 wt% with varying CS concentration, after 24 h of extraction.

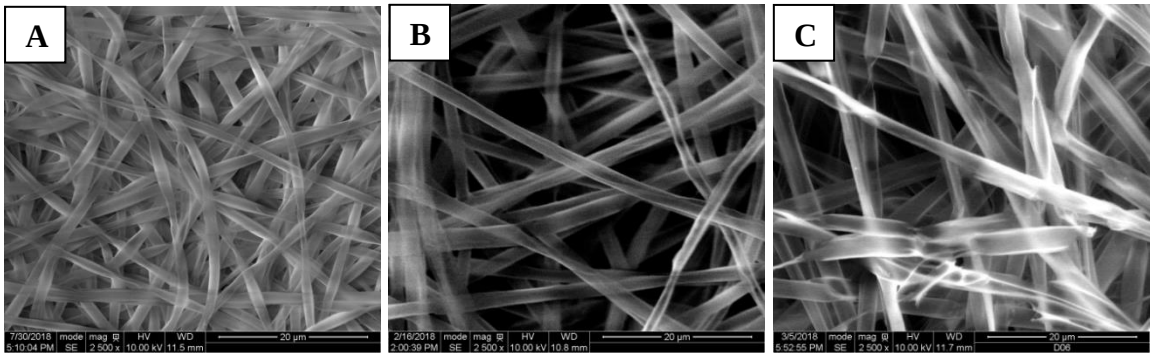

Figure 22: SEM images of fibres produced using shell solution composition of 9 wt % after 24 h of extraction: A) 30, B) 33 and C) 35 wt% core solution.

It can be seen in Figure 22 that at higher concentrations of polystyrene a mixture of cylindrical and flat fibres is obtained. As the concentration of polystyrene in the core increases, the time for extraction also rises. Amongst these combinations, 9 wt% / 30 wt% (shell/core) required the least amount of time for polystyrene extraction and formed flat fibres within 24 hrs.

The images below show fibres obtained at a fixed CS concentration of 30 wt% and varying SS concentration after 24 h of extraction.

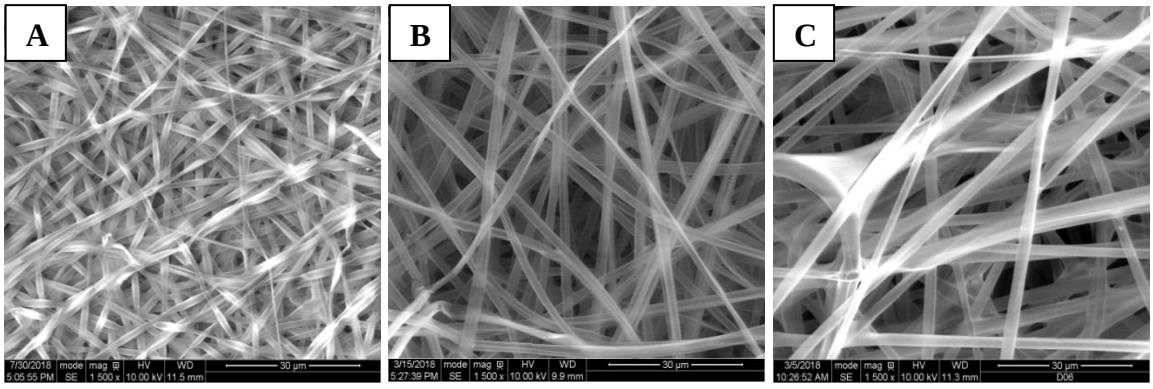

Figure 23: SEM images of fibres produced using core solution composition of 30 wt % after 24 h of extraction: A) 9, B) 12 and C) 13.5 wt% shell solution.

At SS concentrations of 12wt% and 13.5wt% a mixture of cylindrical and flat fibres can be seen in Figure 23. A higher concentration of PAN solution may have led to a thicker shell and thereby increase the time required for polystyrene to diffuse out completely. Thus, a mixture of cylindrical and flat fibres was obtained at these higher SS concentrations.

Although only the 9 wt% / 30 wt% (shell/core) combination produced almost all flat fibres in a period of 24 h, all flat fibres of varying width were produced at the other concentrations of SS and CS when the extraction time was increased from 24 to 72 h. Based on these results, fibres produced using 9 wt% / 30 wt% (shell/core) concentration which require the shortest extraction time were chosen for detailed study of their properties.

4.2 Characterization of Flat Fibre Electrodes

In this section, the material is analysed further and characterized for various physical, transport and structural properties.

4.2.1 Fibre Size

Table 4: Size of various fibres

Fibre diameter (d_f) or Fibre Width (w_f) in µm	**Freudenberg (d_f)**	**Composite Cylindrical Fibres (d_f)**	**Uncarbonized Flat Fibres (w_f)**	**Carbonized Flat Fibres (w_f)**
	10.1 ± 0.3	1.3 ± 0.1	1.5 ± 0.1	0.8 ± 0.1

Freudenberg is a commercial electrode having large fibres of size 10.1 ± 0.3 µm. Electrospinning is an easy technique to make small fibres ranging from nm to micron size. Coaxial electrospinning of PAN/DMF and PS/DMF solutions helped in producing composite cylindrical fibres of diameter 1.3 ± 0.1 µm. As shown in Table 4 and Figure 24, these fibres are much smaller than the Freudenberg sample.

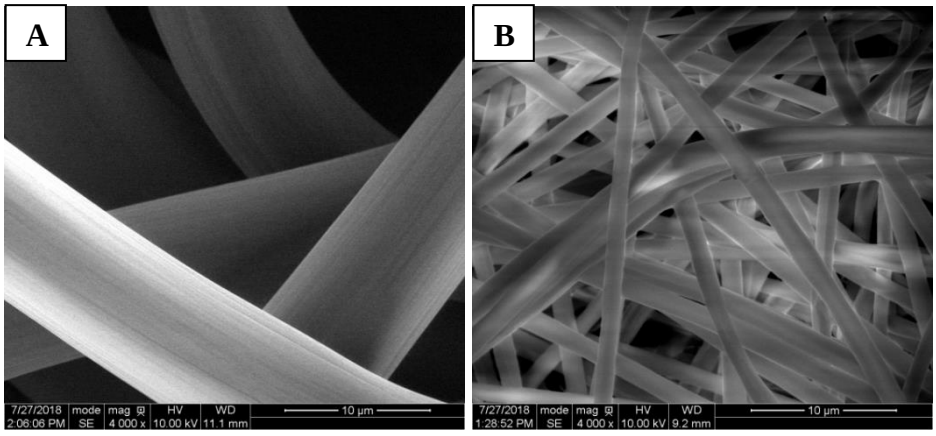

Figure 24: A) Freudenberg fibres and B) electrospun composite cylindrical fibres at the same magnification.

According to the filament analogue model presented in Eqn (8), SA(m^2/m^3) is inversely proportional to the fibre diameter. Thus, the smaller the fibre diameter, the larger will be the surface area per unit volume. However, small diameter fibres result in lower permeability, as illustrated by the Carmen-Kozeny equation. Thus, the coaxially electrospun fibres are expected to provide higher SA and lower permeability than the Freudenberg sample. After extraction of PS from the core of composite cylindrical fibres, the shell collapses to form flat fibres having width greater than the diameter of cylindrical fibres. The images below are of flat fibres formed after extraction.

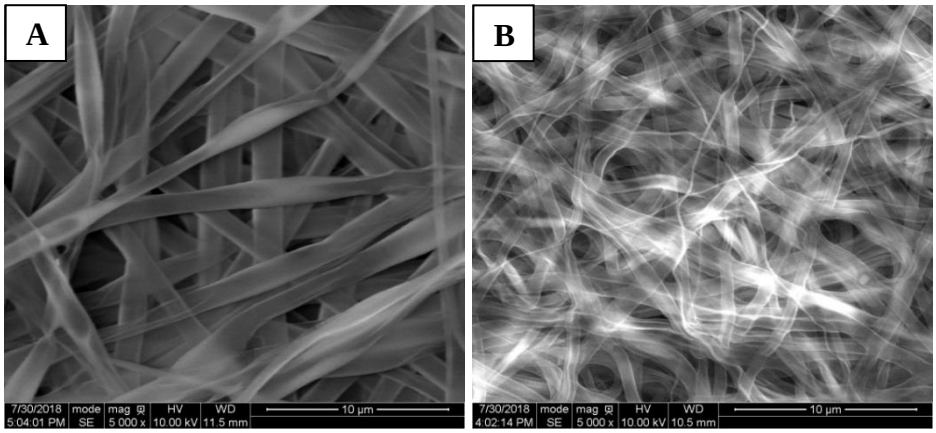

Figure 25: A) Uncarbonized flat fibres and B) carbonized flat fibres.

The uncarbonized and carbonized flat fibres have a width of 1.5 ± 0.1 µm and 0.8 ± 0.1 µm, respectively. Carbonization reduces some of the fibre mass and width. Thus, carbonized flat fibres are smaller than uncarbonized flat fibres.

4.2.2 Porosity

Table 5: Porosity of different fibre samples

Porosity	**Freudenberg**	**Composite Cylindrical Fibres**	**Uncarbonized Flat Fibres**	**Carbonized Flat Fibres**
	0.725 ± 0.00	0.907 ± 0.02	0.862 ± .01	0.926 ± 0.01

The Freudenberg sample has a much lower porosity than the composite cylindrical fibres. In principle, porosity should be independent of fibre size and depend only on the fibre arrangement. The difference seen here therefore is due to the packing density of fibres in the various samples. Despite SEM images of the flat fibres suggesting they were rather tightly packed, their high porosity suggests otherwise. Freudenberg materials are hydro-entangled, explaining their lower porosity.

The porosity of the uncarbonized flat fibres is slightly lower than that of the composite cylindrical fibres because the collapse of the cylindrical fibres to form flat fibres causes them to pack more closely together. The carbonized flat fibres have a higher porosity

than uncarbonized flat fibres due to the removal of solid material and volume during carbonization.

4.2.3 Surface Area

Table 6: Surface area of different fibrous samples

Parameter	Freudenberg	Composite Cylindrical Fibres	Uncarbonized Flat Fibres	Carbonized Flat Fibres
Specific Surface Area (m^2/g)	NIL	25.9	29.3	42.6
Density (kg/m^3)	477.5	98.2	151.2	95.2
Surface Area (m^2/m^3)	108,824.7	2,544,456.4	4,430,704.3	4,056,777.5

The specific surface area (m^2/g) of composite cylindrical fibres is 25.9 m^2/g, whereas that of uncarbonized flat fibres is 29.3 m^2/g. Although the external surface areas of the cylindrical and flat fibres are similar, the decrease in mass of flat fibres due to extraction of polymer from the core is the reason for their higher specific surface area. The specific SA of the carbonized flat fibres is much higher than that of the uncarbonized flat fibres because of the mass lost during carbonization. However, of more importance is the surface area per unit volume (m^2/m^3) since it defines the capacity of the electrode per unit volume. Moreover, this allows for the comparison of materials with different density, specifically the carbonized and uncarbonized samples. The results in Table 6 show that carbonization does not actually add surface area and merely reduces the mass of the fibres.

The surface areas per unit volume of the composite cylindrical fibres and uncarbonized flat fibres are 2,544,456.4 and 4,430,704.3 m^2/m^3, respectively. Changing the fibre morphology from cylindrical to flat increased the SA/volume by a factor of 1.74. This shows the crucial role that the electrode structure plays in improving its physical properties and also in improving battery performance. The SA/volume of carbonized flat fibres is

slightly less than that of uncarbonized flat fibres because carbonization reduces some mass and fibre width, consequently decreasing the surface area of the fibre.

The specific SA of the Freudenberg sample was below the detection limit of the device. Thus, the filament analogue model given in Eqn (8) was used to estimate the SA/volume of the Freudenberg sample to be 108,824.7 m^2/m^3. The SA/volume of the flat fibres is much higher than that of Freudenberg sample because of the difference in fibre morphology and fibre size. This shows that flat fibre electrodes can offer more surface area per unit volume of the electrode for the reaction to take place. This should contribute to higher reaction rates. It is important to note that the filament analogue model is not very accurate and underestimates the surface area of other samples considerably.

4.2.4 Electrical Conductivity

The conductivity of the flat fibre electrode is 2010 S/m in one direction and 1418 S/m in the other direction. The conductivity of Freudenberg is 6126 S/m in one direction and 2114 S/m in the other direction. This shows that our electrospun electrodes are nearly isotropic whereas the commercially available Freudenberg samples are anisotropic. This presumably comes from the manufacturing of the commercial material which is done on a conveyor line. The lower porosity of Freudenberg sample is one of the reasons why they are more conductive than the flat fibre electrodes. Another reason for their higher conductivity is that they are probably made of high quality graphitized carbon. Due to the maximum temperature limit of the tube furnace in the lab, the flat fibre electrode could not be carbonized above 1500°C. Presumably, heating the flat fibre electrodes to a higher temperature of up to 3000°C would have changed their structure to the more conductive graphite. Nonetheless, the conductivity of the flat fibre materials is still quite high, more than sufficient for a flow battery because most ohmic losses occur in the electrolyte.

4.2.5 Permeability

The permeability coefficient is a fitted parameter obtained by application of Darcy's law to flow vs pressure drop experiments. The figure below shows the permeability coefficient for the flat fibre samples in their various states compared to the Freudenberg material.

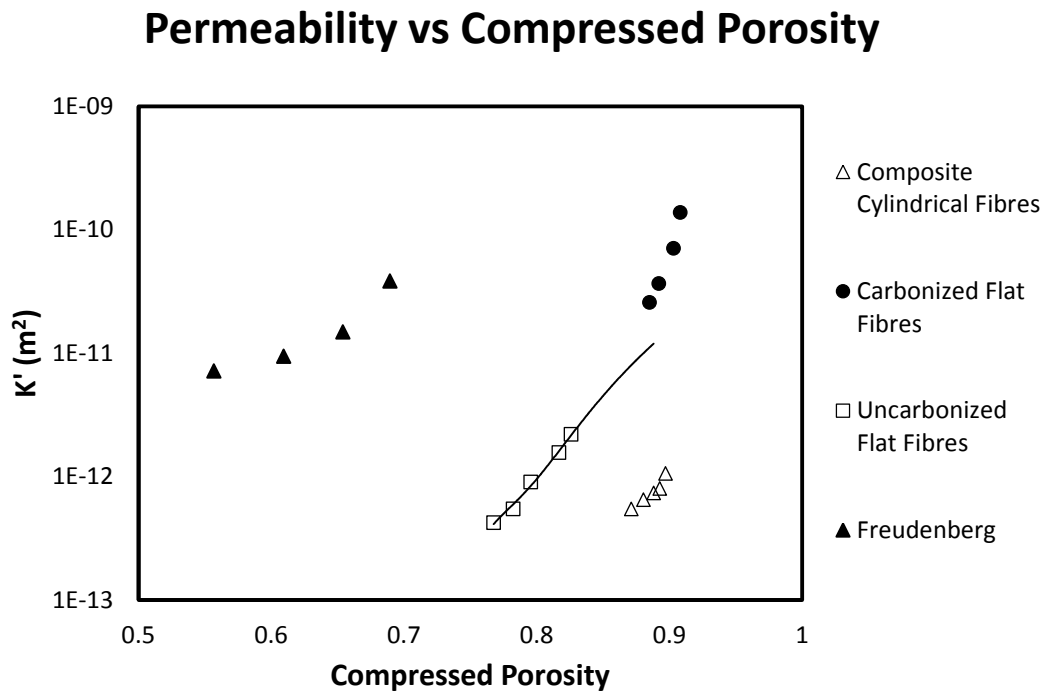

Figure 26: Permeability versus compressed porosity of the various fibres investigated in this study.

It is difficult to compare these materials directly because they have different porosities and sizes. The Carman-Kozeny model is typically used to normalize these sort of data, but it cannot be applied here since it requires knowledge of a fibre diameter which is not defined for the flat fibres (which have a width and thickness that differ substantially). Instead of direct comparison, Figure 26 can be used to track the evolution of the material during the various stages of its processing. The cylindrical composite fibres lie in the bottom right corner of the plot with high porosity but low permeability. Upon extraction of the core, the porosity is reduced as the fibres collapsed and moved closer to each other. The permeability

increased somewhat as well, but the main finding is that the behaviour of these fibres lies on a completely different trend line shifted to the left. Upon carbonization, the porosity and permeability both increase and the data points now cluster in the top right of the plot. The points still lie on the same trend line as the uncarbonized flat fibres, which is expected since the morphology was mostly unchanged by carbonization.

It is encouraging from the graph that the permeability of uncarbonized flat fibres is much higher than that of composite cylindrical fibres for a given porosity. Permeability takes into account various transport properties such as pore size, fibre size, porosity and tortuosity. Cylindrical fibres contain more tortuous pathways for mass transport compared to flat fibres. This could be the reason behind the significant increase in permeability when fibre morphology changes from cylindrical to flat. The black solid dots in Figure 27 (a) represent cross-sections of cylindrical fibres and the flow path illustrated is clearly tortuous. If these cylindrical fibres

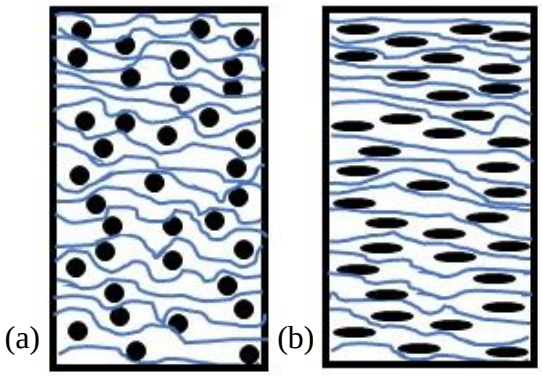

Figure 27: Tortuous path offered by: (a) cylindrical fibres and (b) flat fibres.

collapse into flat fibres, then the path would be less tortuous as shown in Figure 27 (b). Probably the decrease in tortuosity was more significant than the decrease in porosity that led to higher permeability on changing fibre morphology.

The permeability of the Freudenberg sample behaves much differently than that of the electrospun materials, showing far less dependence of permeability on compression.

Presumably, since its fibres and pores are much larger, the voids remain large even as the material is compressed and so the permeability is not strongly affected.

4.3 Vanadium Flow Battery Performance

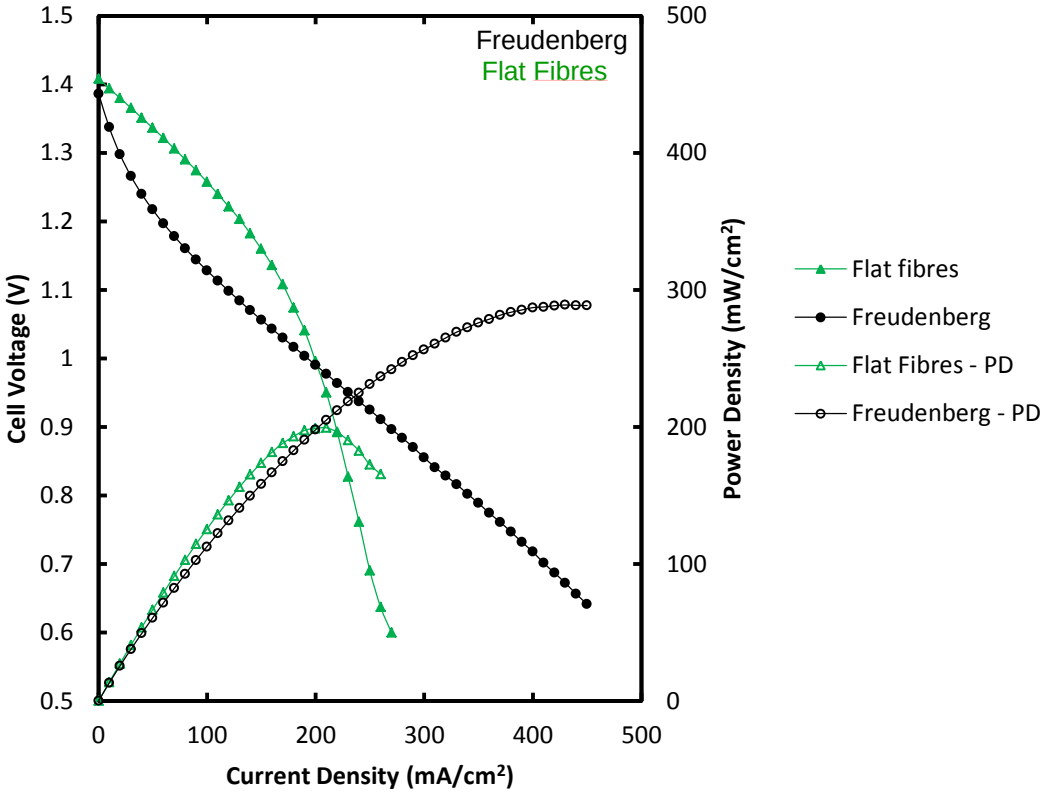

Figure 28: All-vanadium flow battery performance. Polarization and power curves at 50% SOC.

Figure 28 shows polarization and power density curves for flat fibre electrodes and Freudenberg electrode, at 50% SOC. As shown in the graph, up to a current density of 190 mA/cm^2, the voltage drop for flat fibre electrodes is lower than Freudenberg electrode. Therefore resulting in a higher power density of flat fibre electrodes up to 190 mA/cm^2. The reason can be attributed to their higher volumetric surface area which lowers activation losses that dominate at low current densities. However at current densities greater than 190 mA/cm^2, the voltage drop for flat fibres is rapid compared to Freudenberg indicating poor mass transfer in flat fibre electrodes. Freudenberg has large fibres and therefore larger pores allowing for easy transport of reactants to

the active sites. But the small fibre and pore size of flat fibre electrodes hinders mass transfer. It's also possible that the flat fibres are so densely packed in some locations leaving no pore space for electrolyte to flow from one end of the electrode to another, thus adversely affecting mass transfer and its performance.

5 Development and Analysis of Aligned Fibre Electrodes

Electrodes with aligned fibres are of interest because of their high permeability in the direction of fibre alignment. These fibres are prepared by increasing the speed of the rotating drum. These aligned fibres are cylindrical in shape. Cell assembly can be designed appropriately to benefit from the high permeability of an aligned fibre electrode. This can help improve mass transport in electrodes and reduce concentration losses that are observed at high current density. This in turn would lower pumping costs for a given flow rate. Aligned fibres were characterized for various properties given below.

5.1 Detailed Characterization of Fibres

5.1.1 Fibre Diameter

The fibre diameters of uncarbonized and carbonized fibres are 1.4 $\pm$ 0.2 µm and 0.5 $\pm$ 0.1 µm, respectively. The significant decrease in the fibre diameter is due to the mass lost during carbonization.

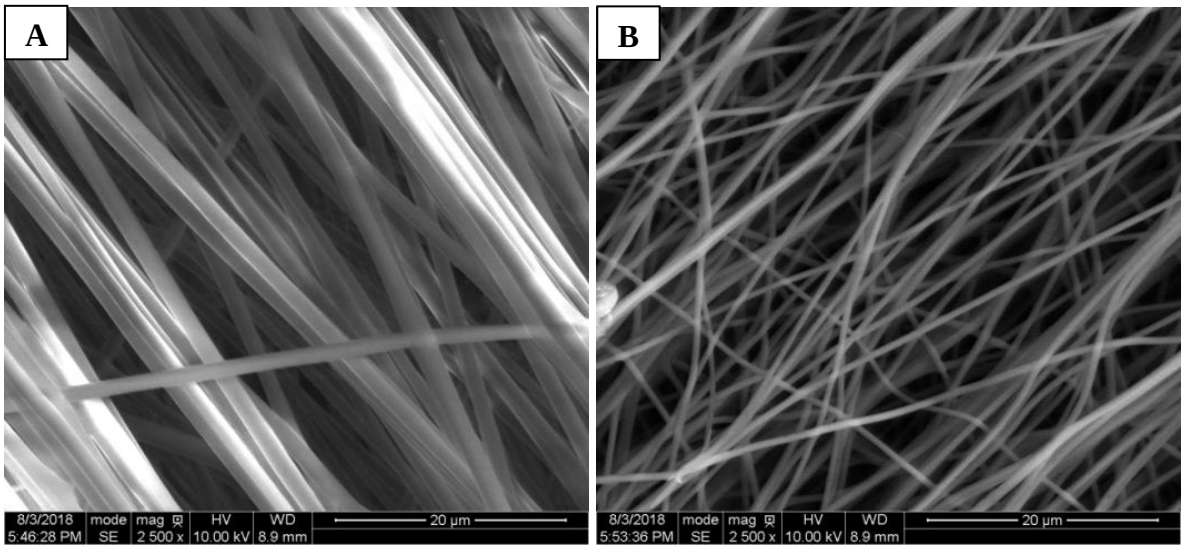

Figure 29: A) Uncarbonized aligned fibres and B) carbonized aligned fibres.

5.1.2 Porosity

The porosities of uncarbonized and carbonized fibres are 83.8% and 93.9%, respectively. This effect of carbonization on porosity is similar to that shown earlier in section 4.2.2. The increase in pore volume of aligned fibres after carbonization can be clearly seen in the SEM images shown in Figure 29.

5.1.3 Surface Area

The surface area of the uncarbonized aligned fibres are compared to that of uncarbonized flat fibres in Table 7 below (Note that carbonization does not increase the volumetric surface area). The aligned fibres show slightly higher surface area per unit volume than the non-aligned flat fibres. The lower porosity of aligned fibres indicates that they have a higher packing density and therefore have a higher SA/volume than the flat fibres.

Table 7: Comparison of surface area of uncarbonized aligned and non-aligned flat fibres

	Porosity	**m^2/g**	**m^2/m^3**
Flat Fibres	86.2%	29.3	4,430,704.3
Aligned Fibres	83.8%	23.8	4,600,000.0

5.1.4 Electrical Conductivity

The electrical conductivities of the aligned fibres in the parallel and perpendicular direction are 1056 S/m and 332 S/m. This anisotropy is expected since electron transport in the direction of fibre alignment is less hindered. In the perpendicular direction, the solid-to-solid contact or fibre-to-fibre contact is minimal leading to lower electrical conductivity in this direction. Overall, the sample shows a lower conductivity than the non-aligned flat fibre material despite similar porosity due to the smaller fibres and the generally fewer connecting pathways between fibres. These conductivity values, especially in the cross-direction, are

becoming low enough to negatively affect cell performance. The conductivity that matters for battery applications is in the through-plane direction, which was not measured here, although it should be similar to that in the perpendicular direction here.

5.1.5 Permeability

As expected, the permeability in the direction of fibre alignment was much higher than in the direction perpendicular to the fibre alignment, as shown in the plot below. This effect is observed because the resistance offered to fluid flow is significantly less in the direction of fibre alignment than in the perpendicular direction.

At 79% compressed porosity, the permeability in the direction of fibre alignment is higher than that in the perpendicular direction by a factor of 6.2.

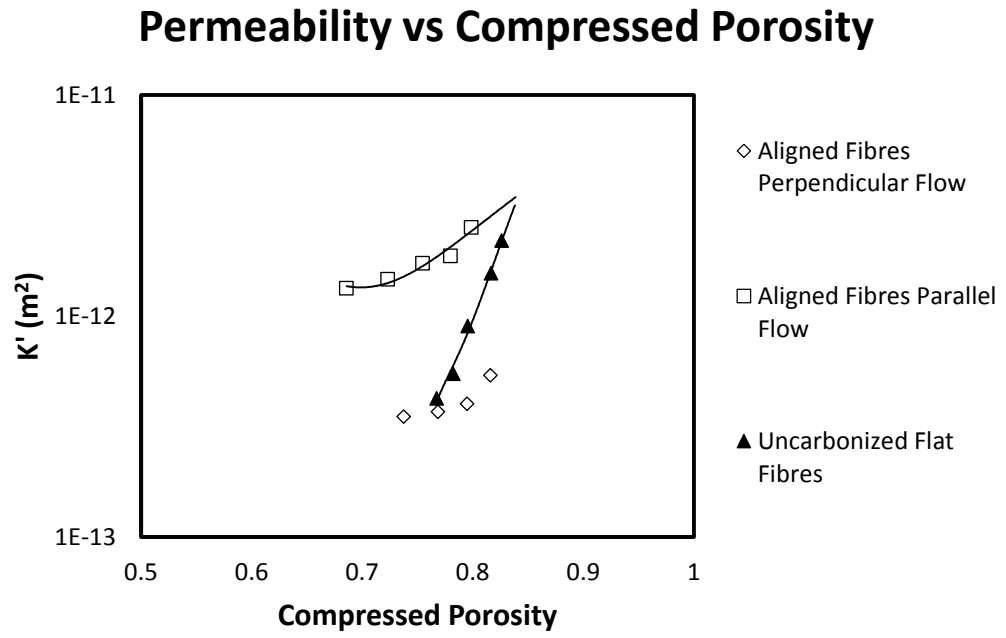

Figure 30: Permeability of aligned fibres in different directions investigated in this study.

For any given compressed porosity, the aligned fibres in the direction of fibre alignment are considerably more permeable than the flat fibres. The permeability of aligned fibres (in the parallel direction) at its uncompressed porosity can be obtained by extrapolating. Uncompressed porosity refers to the actual porosity of the sample obtained

without compressing the sample. However, at the uncompressed porosity of the aligned fibres, the gain in permeability of the aligned fibres is not significant compared to flat fibres.

5.2 Summary

Aligned fibres showed a reasonable set of physical properties such as high surface area, as expected for any electrospun nanofibre material, good permeability in the direction of alignment, but rather low electrical conductivity. This last observation was attributed to the lack of interconnects between the fibres preventing a good conduction network from forming. Another problem not mentioned here is the relatively weak mechanical strength of the aligned materials. This is related to the problem of poor electrical conductivity, namely that insufficient fibres were oriented in the perpendicular direction to bind them together. If a technique could be developed to overcome these challenges, such as interspersing the electrode with layers of randomly oriented fibres, then a promising electrode might be possible.

6 Conclusion and Future Work

6.1 Summary of Results

Flow batteries are a promising device for large scale energy storage because of their separate energy and power components and geographical flexibility. However, power density of flow batteries is lower than that of the well-known lead-acid and lithium-ion batteries. This thesis focused on developing novel flow battery electrodes with the aim of improving the power density of flow batteries. Researchers have made attempts to enhance the power density mostly by modifying the commercially available carbon paper (SGL25AA) which have low reactive surface area and low porosity. Unfortunately, the improvements made so far are not significant. This thesis was aimed at increasing the reactive surface area and enhancing mass transport properties of flow battery electrodes by fabricating them using electrospinning rather than tailoring off-the-shelf material.

Fibrous mats prepared by electrospinning are usually comprised of cylindrical fibres. In the work presented in this thesis, a novel approach was used to change the fibre morphology of electrospun fibres from cylindrical to flat. This yielded an increase in reactive surface area by a factor of 1.6 along with improving permeability by a factor of 35. The increase in reactive surface area was achieved because of the increase in the packing density of the electrode or the surface area per unit volume of the electrode. The improvement in permeability was achieved probably because of the decrease in tortuosity which improved mass transport. The increase in reactive surface area and permeability are known to improve kinetics and decrease concentration losses, respectively thereby making it possible to enhance the power density and performance of flow batteries. In comparison to flat fibre electrodes, the surface area per unit electrode volume of off-the-shelf material (Freudenberg) was lower by a factor of 37. Thus, these flat fibre electrodes have the potential of improving kinetics

more than this off-the-shelf material. Although the electrical conductivity of the flat fibre electrodes was found to be lower than that of the Freudenberg electrode, carbonization at higher temperatures than that conducted in this study can potentially improve their electrical conductivity.

A proof-of-concept was also given for aligned fibres which are expected to offer less resistance to flow in the direction of fibre alignment in comparison to the perpendicular direction. It was observed that at 79% compressed porosity, the permeability in the parallel direction was 6.2 times higher than in the perpendicular direction. At the same time, their electrical conductivity in the perpendicular direction was lower than in the parallel direction because of less solid-solid contact. Further work on producing aligned fibres will be helpful in drawing definite conclusions and optimizing them.

Overall, a novel flow battery electrode was fabricated with improved properties that have the potential of improving flow battery power density and performance.

6.2 Recommendations for Future Work

The flow battery performance results depicted the need to tackle the poor mass transfer in flat fibre electrodes. X-ray tomography of these electrodes will allow to have a look at the fibres present beneath the top surface and gain in-depth understanding of the fibre structure and their mass transfer properties. Improving permeability of flat fibres by producing fibres larger than 1.3 µm in diameter can enhance the flow of reactants and also increase their availability at active sites consequently reducing concentration losses at high current densities. The results from X-ray tomography will provide an opportunity to further optimize these electrodes. Ohmic losses in a battery depend upon the contact between various cell components. The thickness of carbonized materials is not entirely uniform which poses a challenge of uniform compression when the cell is assembled. Thus, work directed on

preparing electrodes with uniform thickness can help in overcoming the challenge of contact resistance between cell components.

There is significant scope to improving the electrical conductivity of the flat fibre electrodes. Carbonizing these electrodes to higher temperature can help reduce electrical resistance by increasing the carbon content of the electrodes and by changing their structure to graphitic [111]. The electrical conductivity can also be enhanced by mixing graphene oxide in the polymer solution before electrospinning. Graphene is highly conducting and thus electrospun fibres consisting graphene will improve the electrical conductivity of the electrodes [112], [113].

Although this thesis focused on improving kinetics by increasing reactive surface area, chemical and thermal treatment of the fibres can further enhance their electrocatalytic activity [114].

A problem that was faced in the work presented was the brittleness of the electrode. It is known that incomplete reactions during the stabilization process can make the electrode brittle. Thus, when the duration of the stabilization step was increased from 75 minutes to 3 hours during carbonization, the resulting electrodes became more flexible. However, a more detailed study of the carbonization process would be helpful in producing electrodes that are more flexible.

Continuous improvements in the electrode structure by optimizing its surface area and mass transport properties can help in making suitable electrodes for flow batteries and thus improve their performance and accelerate their commercialization.

7 References

[1] "Global Energy & CO2 Status Report," 2017. [Online]. Available: https://www.iea.org/publications/freepublications/publication/GECO2017.pdf. [Accessed: 17-Aug-2018].

[2] "World electricity generation from 1990-1995," 2018. [Online]. Available: https://www.statista.com/statistics/270281/electricity-generation-worldwide/. [Accessed: 17-Aug-2018].

[3] A. Z. Weber, M. M. Mench, J. P. Meyers, P. N. Ross, J. T. Gostick, and Q. Liu, "Redox flow batteries: A review," *J. Appl. Electrochem.*, vol. 41, no. 10, pp. 1137–1164, 2011.

[4] M. Skyllas-Kazacos, M. H. Chakrabarti, S. A. Hajimolana, F. S. Mjalli, and M. Saleem, "Progress in Flow Battery Research and Development," *J. Electrochem. Soc.*, vol. 158, no. 8, p. R55, 2011.

[5] L. Li *et al.*, "A stable vanadium redox-flow battery with high energy density for large-scale energy storage," *Adv. Energy Mater.*, vol. 1, no. 3, pp. 394–400, 2011.

[6] X. Li, H. Zhang, Z. Mai, H. Zhang, and I. Vankelecom, "Ion exchange membranes for vanadium redox flow battery (VRB) applications," *Energy Environ. Sci.*, vol. 4, no. 4, pp. 1147–1160, 2011.

[7] K. Lin *et al.*, "Alkaline quinone flow battery.," *Science*, vol. 349, no. 6255, pp. 1529–32, Sep. 2015.

[8] P. Alotto, M. Guarnieri, and F. Moro, "Redox flow batteries for the storage of renewable energy: A review," *Renew. Sustain. Energy Rev.*, vol. 29, pp. 325–335, 2013.

[9] S. Liu, "Production and Characterization of Novel Flow Battery Electrodes via Electrospinning," MASc Thesis, McGill University, 2017.

[10] Z. Qi and G. M. Koenig, "Review Article: Flow battery systems with solid electroactive materials," *J. Vac. Sci. Technol. B*, vol. 35, no. 4, 2017.

[11] M. H. Chakrabarti *et al.*, "Application of carbon materials in redox flow batteries," *J.*

Power Sources, vol. 253, pp. 150–166, 2014.

[12] X. L. Zhou, T. S. Zhao, Y. K. Zeng, L. An, and L. Wei, "A highly permeable and enhanced surface area carbon-cloth electrode for vanadium redox flow batteries," *J. Power Sources*, vol. 329, pp. 247–254, 2016.

[13] A. M. Pezeshki, J. T. Clement, G. M. Veith, T. A. Zawodzinski, and M. M. Mench, "High performance electrodes in vanadium redox flow batteries through oxygen-enriched thermal activation," *J. Power Sources*, vol. 294, pp. 333–338, 2015.

[14] X. L. Zhou, Y. K. Zeng, X. B. Zhu, L. Wei, and T. S. Zhao, "A high-performance dual-scale porous electrode for vanadium redox flow batteries," *J. Power Sources*, vol. 325, pp. 329–336, 2016.

[15] M. D. R. Kok, A. Khalifa, and J. T. Gostick, "Multiphysics Simulation of the Flow Battery Cathode: Cell Architecture and Electrode Optimization," *J. Electrochem. Soc.*, vol. 163, no. 7, pp. A1408–A1419, 2016.

[16] R. R. Rashapov, J. Unno, and J. T. Gostick, "Characterization of PEMFC Gas Diffusion Layer Porosity," *J. Electrochem. Soc.*, vol. 162, no. 6, pp. F603–F612, 2015.

[17] S. Liu, M. Kok, Y. Kim, J. L. Barton, F. R. Brushett, and J. Gostick, "Evaluation of Electrospun Fibrous Mats Targeted for Use as Flow Battery Electrodes," *J. Electrochem. Soc.*, vol. 164, no. 9, pp. A2038–A2048, 2017.

[18] M. Aneke and M. Wang, "Energy storage technologies and real life applications – A state of the art review," *Appl. Energy*, vol. 179, pp. 350–377, 2016.

[19] H. L. Ferreira, R. Garde, G. Fulli, W. Kling, and J. P. Lopes, "Characterisation of electrical energy storage technologies," *Energy*, vol. 53, pp. 288–298, 2013.

[20] H. Ibrahim, A. Ilinca, and J. Perron, "Energy storage systems-Characteristics and comparisons," *Renew. Sustain. Energy Rev.*, vol. 12, no. 5, pp. 1221–1250, 2008.

[21] T. Kousksou, P. Bruel, A. Jamil, T. El Rhafiki, and Y. Zeraouli, "Energy storage: Applications and challenges," vol. 120,Part A, pp. 59–80, 2013.

[22] H. Blanco and A. Faaij, "A review at the role of storage in energy systems with a focus on Power to Gas and long-term storage," *Renew. Sustain. Energy Rev.*, vol. 81,Part 1,

pp. 1049–1086, 2018.

[23] H. Chen, T. N. Cong, W. Yang, C. Tan, Y. Li, and Y. Ding, “Progress in electrical energy storage system: A critical review,” *Prog. Nat. Sci.*, vol. 19, no. 3, pp. 291–312, 2009.

[24] A. Ozarslan, “Large-scale hydrogen energy storage in salt caverns,” *Int. J. Hydrogen Energy*, vol. 37, no. 19, pp. 14265–14277, 2012.

[25] “North American Clean Energy - Hydrogen Electrolysis as a Viable Solution for Large Scale Renewable Energy Storage.” [Online]. Available: http://www.nacleanenergy.com/articles/29771/hydrogen-electrolysis-as-a-viable-solution-for-large-scale-renewable-energy-storage. [Accessed: 17-Aug-2018].

[26] M. Melaina and J. Eichman, “Hydrogen Energy Storage: Grid and Transportation Services.” [Online]. Available: https://www.nrel.gov/docs/fy15osti/62518.pdf. [Accessed: 17-Aug-2018].

[27] M. Schiller, “Hydrogen Energy Storage: A New Solution To the Renewable Energy Intermittency Problem - Renewable Energy World,” 2014. [Online]. Available: https://www.renewableenergyworld.com/articles/2014/07/hydrogen-energy-storage-a-new-solution-to-the-renewable-energy-intermittency-problem.html. [Accessed: 14-Sep-2018].

[28] O. Schmidt, A. Gambhir, I. Staffell, A. Hawkes, J. Nelson, and S. Few, “Future cost and performance of water electrolysis: An expert elicitation study,” *Int. J. Hydrogen Energy*, vol. 42, no. 52, pp. 30470–30492, 2017.

[29] S. Vazquez, S. M. Lukic, E. Galvan, L. G. Franquelo, and J. M. Carrasco, “Energy Storage Systems for Transport and Grid Applications,” vol. 57, no. 12, pp. 3881–3895, 2010.

[30] C. D. Wessells, M. T. McDowell, S. V. Peddada, M. Pasta, R. A. Huggins, and Y. Cui, “Tunable Reaction Potentials in Open Framework Nanoparticle Battery Electrodes for Grid-Scale Energy Storage,” *ACS Nano*, vol. 6, no. 2, pp. 1688–1694, 2012.

[31] J. Liu *et al.*, “Materials science and materials chemistry for large scale electrochemical energy storage: From transportation to electrical grid,” *Adv. Funct. Mater.*, vol. 23, no.

8, pp. 929–946, 2013.

[32] S. Koohi-Kamali, V. V. Tyagi, N. A. Rahim, N. L. Panwar, and H. Mokhlis, "Emergence of energy storage technologies as the solution for reliable operation of smart power systems: A review," *Renew. Sustain. Energy Rev.*, vol. 25, pp. 135–165, 2013.

[33] H. Zheng, J. Li, X. Song, G. Liu, and V. S. Battaglia, "A comprehensive understanding of electrode thickness effects on the electrochemical performances of Li-ion battery cathodes," *Electrochim. Acta*, vol. 71, pp. 258–265, 2012.

[34] R. Zhao, J. Liu, and J. Gu, "The effects of electrode thickness on the electrochemical and thermal characteristics of lithium ion battery," *Appl. Energy*, vol. 139, pp. 220–229, 2015.

[35] M. R. Mohamed, S. M. Sharkh, and F. C. Walsh, "Redox flow batteries for hybrid electric vehicles: Progress and challenges," *5th IEEE Veh. Power Propuls. Conf. VPPC '09*, pp. 551–557, 2009.

[36] B. R. Chalamala, T. Soundappan, G. R. Fisher, M. R. Anstey, V. V. Viswanathan, and M. L. Perry, "Redox flow batteries: An engineering perspective," *Proc. IEEE*, vol. 102, no. 6, pp. 976–999, 2014.

[37] P. Nikolaidis and A. Poullikkas, "Cost metrics of electrical energy storage technologies in potential power system operations," *Sustain. Energy Technol. Assessments*, vol. 25, pp. 43–59, 2018.

[38] K. J. Kim, M.-S. Park, Y.-J. Kim, J. H. Kim, S. X. Dou, and M. Skyllas-Kazacos, "A technology review of electrodes and reaction mechanisms in vanadium redox flow batteries," *J. Mater. Chem. A*, vol. 3, no. 33, pp. 16913–16933, 2015.

[39] "Integrating Renewable Electricity on the Grid A Report by the APS Panel on Public Affairs," *American Physical Society*, 2010. [Online]. Available: https://www.aps.org/policy/reports/popa-reports/upload/integratingelec.pdf. [Accessed: 14-Sep-2018].

[40] W. Kangro, "Method for storing electrical energy," DE914264C, 28–Jun–1949.

[41] J. Winsberg, T. Hagemann, T. Janoschka, M. D. Hager, and U. S. Schubert, "Redox-

Flow Batteries: From Metals to Organic Redox-Active Materials," *Angew. Chemie - Int. Ed.*, vol. 56, pp. 686–711, 2017.

[42] T. Nguyen and R. F. Savinell, "Flow Batteries," 2010. [Online]. Available: http://large.stanford.edu/courses/2011/ph240/garg1/docs/fal10_p054-056.pdf. [Accessed: 17-Aug-2018].

[43] F. Pan and Q. Wang, "Redox species of redox flow batteries: A review," *Molecules*, vol. 20, no. 11, pp. 20499–20517, 2015.

[44] K. Wedege, E. Dražević, D. Konya, and A. Bentien, "Organic Redox Species in Aqueous Flow Batteries: Redox Potentials, Chemical Stability and Solubility," *Sci. Rep.*, vol. 6, no. 1, p. 39101, Dec. 2016.

[45] X. Wei *et al.*, "Materials and Systems for Organic Redox Flow Batteries: Status and Challenges," *Am. Chem. Soc.*, vol. 2, no. 9, pp. 2187–2204, 2017.

[46] C. Ponce de León, A. Frías-Ferrer, J. González-García, D. A. Szánto, and F. C. Walsh, "Redox flow cells for energy conversion," *J. Power Sources*, vol. 160, no. 1, pp. 716–732, 2006.

[47] L. Su, J. A. Kowalski, K. J. Carroll, and F. R. Brushett, "Recent Developments and Trends in Redox Flow Batteries," *Recharg. Batter.*, pp. 673–712, 2015.

[48] M. Duduta *et al.*, "Semi-solid lithium rechargeable flow battery," *Adv. Energy Mater.*, vol. 1, no. 4, pp. 511–516, 2011.

[49] G. Kaur, "Cell Voltages, Polarisations and Performances," *Solid Oxide Fuel Cell Components*, pp. 43–78, 2016.

[50] K. J. Yoon, S. Gopalan, and U. B. Pal, "Effect of Fuel Composition on Performance of Single-Step Cofired SOFCs," *J. Electrochem. Soc.*, vol. 154, no. 10, pp. B1080–B1087, 2007.

[51] D. Aaron, Z. Tang, A. B. Papandrew, and T. A. Zawodzinski, "Polarization curve analysis of all-vanadium redox flow batteries," *J. Appl. Electrochem.*, vol. 41, pp. 1175–1182, 2011.

[52] T. Davies and J. Tummino, "High-Performance Vanadium Redox Flow Batteries with

Graphite Felt Electrodes," *C*, vol. 4, no. 1, 2018.

[53] J. Houser, A. Pezeshki, J. T. Clement, D. Aaron, and M. M. Mench, "Architecture for improved mass transport and system performance in redox flow batteries," *J. Power Sources*, vol. 351, pp. 96–105, 2017.

[54] A. E. SCHEIDEGGER, "The Physics of Flow Through Porous Media," *Soil Sci.*, vol. 86, no. 6, 1958.

[55] S. Sunjai Nakshatharan, A. Punning, U. Johanson, and A. Aabloo, "Effect of porosity and tortuosity of electrodes on carbon polymer soft actuators," *J. Appl. Phys.*, vol. 123, no. 1, 2018.

[56] B. Tjaden, D. J. L. Brett, and P. R. Shearing, "Tortuosity in electrochemical devices: a review of calculation approaches," *Int. Mater. Rev.*, vol. 63, no. 2, pp. 47–67, 2018.

[57] A. Tang, J. Bao, and M. Skyllas-Kazacos, "Studies on pressure losses and flow rate optimization in vanadium redox flow battery," *J. Power Sources*, vol. 248, pp. 154–162, 2014.

[58] C. Zhang, T. S. Zhao, Q. Xu, L. An, and G. Zhao, "Effects of operating temperature on the performance of vanadium redox flow batteries," vol. 155, pp. 349–353, 2015.

[59] A. Su, Y. M. Ferng, and C. B. Wang, "Investigating parametric effects on performance of a high-temperature URSOFC," *Int. J. Energy Res.*, vol. 39, no. 5, pp. 648–660, 2015.

[60] H. R. Wengrow, "Mass Transfer In Porous Gas Diffusion Electrodes," University of Florida, 1963.

[61] M. Ben Clennell, "Tortuosity: a guide through the maze," *Geol. Soc. Publ.*, vol. 122, pp. 299–344, 1997.

[62] M. D. R. Kok and J. T. Gostick, "Transport properties of electrospun fibrous membranes with controlled anisotropy," *J. Memb. Sci.*, vol. 473, pp. 237–244, Jan. 2015.

[63] V. Gurau, M. J. Bluemle, E. S. De Castro, Y.-M. Tsou, T. A. Zawodzinski, and J. A. Mann, "Characterization of transport properties in gas diffusion layers for proton

exchange membrane fuel cells 2. Absolute permeability," *J. Power Sources*, vol. 165, pp. 793–802, 2007.

[64] P. Mangal *et al.*, "Experimental study of mass transport in PEMFCs: Through plane permeability and molecular diffusivity in GDLs," *Electrochim. Acta*, vol. 167, pp. 160–171, 2015.

[65] K. Yazdchi, S. Srivastava, and S. Luding, "On the Validity of the Carman-Kozeny Equation in Random Fibrous Media," *II Int. Conf. Part. Methods - Fundam. Appl.*, pp. 1–10, 2011.

[66] N. Bhardwaj and S. C. Kundu, "Electrospinning: A fascinating fiber fabrication technique," *Biotechnol. Adv.*, vol. 28, no. 3, pp. 325–347, 2010.

[67] A. Frenot and I. S. Chronakis, "Polymer nanofibers assembled by electrospinning," *Curr. Opin. Colloid Interface Sci.*, vol. 8, no. 1, pp. 64–75, 2003.

[68] J. V. Patil, S. S. Mali, A. S. Kamble, C. K. Hong, J. H. Kim, and P. S. Patil, "Electrospinning: A versatile technique for making of 1D growth of nanostructured nanofibers and its applications: An experimental approach," *Appl. Surf. Sci.*, vol. 423, pp. 641–674, 2017.

[69] S. Homaeigohar, Y. Davoudpour, Y. Habibi, and M. Elbahri, "The Electrospun Ceramic Hollow Nanofibers," *Nanomaterials*, vol. 7, no. 11, p. 383, Nov. 2017.

[70] S. Sakuldao, T. Yoovidhya, and S. Wongsasulak, "Coaxial electrospinning and sustained release properties of gelatin-cellulose acetate core-shell ultrafine fibres," *ScienceAsia*, vol. 37, pp. 335–343, 2011.

[71] R. Khajavi and M. Abbasipour, "Electrospinning as a versatile method for fabricating coreshell, hollow and porous nanofibers," *Sci. Iran.*, vol. 19, no. 6, pp. 2029–2034, 2012.

[72] Wahyudiono, S. Machmudah, H. Kanda, S. Okubayashi, and M. Goto, "Formation of PVP hollow fibers by electrospinning in one-step process at sub and supercritical CO2," *Chem. Eng. Process. Process Intensif.*, vol. 77, pp. 1–6, 2014.

[73] B. Binfei ZHANG and M. Chang, "Curled Poly(ethylene glycol terephthalate)/ Poly(ethylene propanediol terephthalate) Nanofibers Produced by Side-by-side

Electrospinning," *Polym. J.*, vol. 41, pp. 252–252, 2009.

[74] S. Zaicheng, E. Zussman, A. L. Yarin, J. H. Wendorff, and A. Greiner, "Compound Core-Shell Polymer Nanofibers by Co-Electrospinning," *Adv. Mater.*, vol. 15, no. 22, pp. 1929–1932, 2003.

[75] T. H. Hwang, Y. M. Lee, B. S. Kong, J. S. Seo, and J. W. Choi, "Electrospun core-shell fibers for robust silicon nanoparticle-based lithium ion battery anodes," *Nano Lett.*, vol. 12, no. 2, pp. 802–807, 2012.

[76] F. H. Anka and K. J. Balkus, "Novel nanofiltration hollow fiber membrane produced via electrospinning," *Ind. Eng. Chem. Res.*, vol. 52, no. 9, pp. 3473–3480, 2013.

[77] J. C. Yang *et al.*, "Formation of highly aligned, single-layered, hollow fibrous assemblies and the fabrication of large pieces of PLLA membranes," *Macromol. Mater. Eng.*, vol. 297, no. 2, pp. 115–122, 2012.

[78] Z. Qi, H. Yu, Y. Chen, and M. Zhu, "Highly porous fibers prepared by electrospinning a ternary system of nonsolvent/solvent/poly(l-lactic acid)," *Mater. Lett.*, vol. 63, no. 3–4, pp. 415–418, 2009.

[79] K. A. G. Katsogiannis, G. T. Vladisavljević, and S. Georgiadou, "Porous electrospun polycaprolactone (PCL) fibres by phase separation," *Eur. Polym. J.*, vol. 69, pp. 284–295, 2015.

[80] C. L. Casper, J. S. Stephens, N. G. Tassi, D. B. Chase, and J. F. Rabolt, "Controlling surface morphology of electrospun polystyrene fibers: Effect of humidity and molecular weight in the electrospinning process," *Macromolecules*, vol. 37, no. 2, pp. 573–578, 2004.

[81] J. T. McCann, M. Marquez, and Y. Xia, "Highly porous fibers by electrospinning into a cryogenic liquid," *J. Am. Chem. Soc.*, vol. 128, no. 5, pp. 1436–1437, 2006.

[82] A. Celebioglu and T. Uyar, "Electrospun porous cellulose acetate fibers from volatile solvent mixture," *Mater. Lett.*, vol. 65, no. 14, pp. 2291–2294, 2011.

[83] M. Dhanalakshmi and J. P. Jog, "Preparation and characterization of electrospun fibers of Nylon 11," *Express Polym. Lett.*, vol. 2, no. 8, pp. 540–545, 2008.

[84] S. Koombhongse, W. Liu, and D. H. Reneker, “Flat polymer ribbons and other shapes by electrospinning,” *J. Polym. Sci. Part B Polym. Phys.*, vol. 39, no. 21, pp. 2598–2606, 2001.

[85] F. Topuz and T. Uyar, “Electrospinning of gelatin with tunable fiber morphology from round to flat/ribbon,” *Mater. Sci. Eng. C*, vol. 80, pp. 371–378, Nov. 2017.

[86] N. Amiraliyan, M. Nouri, and M. H. Kish, “Effects of some electrospinning parameters on morphology of Natural silk-based nanofibers,” *J. Appl. Polym. Sci.*, vol. 113, pp. 226–234, 2009.

[87] A. Koski, K. Yim, and S. Shivkumar, “Effect of molecular weight on fibrous PVA produced by electrospinning,” *Mater. Lett.*, vol. 58, no. 3–4, pp. 493–497, 2004.

[88] L. Buttafoco *et al.*, “Electrospinning of collagen and elastin for tissue engineering applications,” *Biomaterials*, vol. 27, no. 5, pp. 724–734, 2006.

[89] R. GOPAL, “Influence of Electrospun Nanofibrous Architecture in Separation Technology,” PhD Thesis, National University of Singapore, 2010.

[90] J. I. Kim, T. I. Hwang, L. E. Aguilar, C. H. Park, and C. S. Kim, “A Controlled Design of Aligned and Random Nanofibers for 3D Bi-functionalized Nerve Conduits Fabricated via a Novel Electrospinning Set-up,” *Sci. Rep.*, 2016.

[91] B. Sundaray, V. Subramanian, T. S. Natarajan, R. Z. Xiang, C. C. Chang, and W. S. Fann, “Electrospinning of continuous aligned polymer fibers,” *Appl. Phys. Lett.*, vol. 84, no. 7, 2004.

[92] K. J. Aviss, J. E. Gough, and S. Downes, “Aligned electrospun polymer fibres for skeletal muscle regeneration,” *Eur. Cells Mater.*, vol. 19, pp. 193–204, 2010.

[93] H. Hou *et al.*, “Electrospun polyacrylonitrile nanofibers containing a high concentration of well-aligned multiwall carbon nanotubes,” *Chem. Mater.*, vol. 17, no. 5, pp. 967–973, 2005.

[94] T. H. Kao, S. K. Su, C. I. Su, A. W. Lee, and J. K. Chen, “Polyacrylonitrile microscaffolds assembled from mesh structures of aligned electrospun nanofibers as high-efficiency particulate air filters,” *Aerosol Sci. Technol.*, vol. 50, no. 6, pp. 615–625, 2016.

[95] P. Katta, M. Alessandro, A. R. D. Ramsier, and G. G. Chase, “Continuous Electrospinning of Aligned Polymer Nanofibers onto a Wire Drum Collector,” vol. 4, no. 111, pp. 2215–2218, 2004.

[96] C. Ayres *et al.*, “Modulation of anisotropy in electrospun tissue-engineering scaffolds: Analysis of fiber alignment by the fast Fourier transform,” *Biomaterials*, vol. 27, no. 32, pp. 5524–5534, 2006.

[97] H. Yuan, Q. Zhou, and Y. Zhang, “Improving fiber alignment during electrospinning,” *Electrospun Nanofibers*, pp. 125–147, 2016.

[98] Z. Zhou *et al.*, “Development of carbon nanofibers from aligned electrospun polyacrylonitrile nanofiber bundles and characterization of their microstructural, electrical, and mechanical properties,” *Polymer (Guildf).*, vol. 50, no. 13, pp. 2999–3006, 2009.

[99] B. Saha and G. C. Schatz, “Carbonization in polyacrylonitrile (PAN) based carbon fibers studied by reaxff molecular dynamics simulations,” *J. Phys. Chem. B*, vol. 116, no. 15, pp. 4684–4692, 2012.

[100] N. Yusof and A. F. Ismail, “Post spinning and pyrolysis processes of polyacrylonitrile (PAN)-based carbon fiber and activated carbon fiber: A review,” *J. Anal. Appl. Pyrolysis*, vol. 93, pp. 1–13, 2011.

[101] J. Meinl, K. Schönfeld, M. Kirsten, K. Kittler, A. Michaelis, and C. Cherif, “Optimization of the temperature program to scale up the stabilization of polyacrylonitrile fibers,” *Compos. Part A Appl. Sci. Manuf.*, vol. 96, pp. 37–45, May 2017.

[102] B. A. Newcomb, “Processing, structure, and properties of carbon fibers,” *Compos. Part A Appl. Sci. Manuf.*, vol. 91, Part 1, pp. 262–282, 2016.

[103] M. S. A. Rahaman, A. F. Ismail, and A. Mustafa, “A review of heat treatment on polyacrylonitrile fiber,” *Polym. Degrad. Stab.*, vol. 92, no. 8, pp. 1421–1432, 2007.

[104] Y. Hou, T. Sun, H. Wang, and D. Wu, “Effect of Heating Rate on the Chemical Reaction during Stabilization of Polyacrylonitrile Fibers,” *Text. Res. J. Artic. Text. Res. J.*, vol. 78, no. 9, pp. 806–811, 2008.

[105] J. T. Gostick, M. W. Fowler, M. D. Pritzker, M. A. Ioannidis, and L. M. Behra, "In-plane and through-plane gas permeability of carbon fiber electrode backing layers," *J. Power Sources*, vol. 162, no. 1, pp. 228–238, 2006.

[106] J. D. Milshtein, J. L. Barton, R. M. Darling, and F. R. Brushett, "4-acetamido-2,2,6,6-tetramethylpiperidine-1-oxyl as a model organic redox active compound for nonaqueous flow batteries," *J. Power Sources*, vol. 327, pp. 151–159, 2016.

[107] J. D. Milshtein, S. L. Fisher, T. M. Breault, L. T. Thompson, and F. R. Brushett, "Feasibility of a Supporting-Salt-Free Nonaqueous Redox Flow Battery Utilizing Ionic Active Materials," *ChemSusChem*, vol. 10, no. 9, pp. 2080–2088, 2017.

[108] D. S. Aaron *et al.*, "Dramatic performance gains in vanadium redox flow batteries through modified cell architecture," *J. Power Sources*, vol. 206, pp. 450–453, 2012.

[109] F. Yalcinkaya, O. Jirsak, and R. Gemci, "Effect of Polymer Concentration on Electrospinning System," *Fiber Soc.*, pp. 1–7, 2010.

[110] J. H. He, Y. Q. Wan, and J. Y. Yu, "Effect of concentration on electrospun polyacrylonitrile (PAN) nanofibers," *Fibers Polym.*, vol. 9, no. 2, pp. 140–142, 2008.

[111] X. Huang, "Fabrication and properties of carbon fibers," *Materials (Basel).*, vol. 2, no. 4, pp. 2369–2403, 2009.

[112] P. Suktha and M. Sawangphruk, "Electrospinning of Carbon–Carbon Fiber Composites for High-Performance Single Coin-Cell Supercapacitors: Effects of Carbon Additives and Electrolytes," *Ind. Eng. Chem. Res.*, vol. 56, no. 36, pp. 10078–10086, Sep. 2017.

[113] "Carbon fibers from electrospinning," 2017. [Online]. Available: http://electrospintech.com/carbonfibers.html#.W3nnF85KjIV. [Accessed: 14-Sep-2018].

[114] C. Xu, X. Yang, X. Li, T. Liu, and H. Zhang, "Ultrathin free-standing electrospun carbon nanofibers web as the electrode of the vanadium flow batteries," *J. Energy Chem.*, vol. 26, no. 4, pp. 730–737, 2017.